MirrorSAR: An HRWS Add-On for Single-Pass Multi-Baseline SAR Interferometry

Josef Mittermayer, Gerhard Krieger, *Fellow, IEEE*, Allan Bojarski, Mariantonietta Zonno,
Michelangelo Villano, *Senior Member, IEEE,* Muriel Pinheiro, Markus Bachmann, Stefan Buckreuss,
and Alberto Moreira, *Fellow, IEEE*

Abstract — This paper reports the Phase A study results of the interferometric extension of the High-Resolution Wide-Swath (HRWS) mission with three MirrorSAR satellites. According to the MirrorSAR concept, small, low cost, transponder-like receive-only satellites without radar signal demodulation, digitization, memory storage, downlink, and synchronization are added to the planned German X-band HRWS mission. The MirrorSAR satellites fly a triple helix orbit in close formation around the HRWS orbit and span multiple single-pass interferometric baselines. A comprehensive system engineering and performance analysis is provided that includes orbit formation, MirrorLink, Doppler steering, antenna pattern and swath design, multi-static echo window timing, SAR performance, height performance and coverage analysis. The overall interferometric system design analysis of Phase A is presented. The predicted performance of the global Digital Elevation Model (DEM) is improved by one order of magnitude compared to presently available global DEM products like the TanDEM-X DEM.

Index Terms—**Digital Elevation Model (DEM), HRWS, Interferometry, MirrorSAR, Synthetic Aperture Radar (SAR).**

I. INTRODUCTION

The High-Resolution Wide-Swath mission (HRWS) [1], [2] is being considered for realization by the Space Agency of the German Aerospace Center (DLR). It consists of the high-end HRWS satellite, which is a fully stand-alone transmit/receive radar system equipped with high transmit power and digital beam-forming with multiple azimuth phase centers [3], [4], [5], [6], so that an azimuth resolution of 25 cm in Spotlight mode with a swath of 25 km can be obtained. Further, high operational flexibility allows for innovative and/or high-performance acquisition modes like the Theater mode, consisting of up to eight quasi-simultaneous spotlight acquisitions in areas of interest, each with 7.5 km × 7.5 km coverage and 25 cm azimuth/range resolution, a stripmap mode with 50 km and 80 km swath with 1 and 3 meter azimuth resolution, respectively, as well as a ScanSAR mode with a maximum swath of 500 km at a range and azimuth resolution of 2 m × 16 m, respectively [1], [2].

During Phase 0/A, the HRWS mission concept has been extended by three small and low-cost receive-only satellites following the MirrorSAR concept that has been developed at the Microwaves and Radar Institute of DLR [23], [24], [25]. MirrorSAR adds multistatic interferometric capability and therefore allows the generation of a DEM.

Given the great demand of the user community for the DEM data of the TanDEM-X mission, HRWS-MirrorSAR also aims at ensuring the continuity of the successful series of German X-band Synthetic Aperture Radar (SAR) missions.

The roadmap of German X-band SAR missions started in 1983 with the Microwave Remote Sensing Experiment (MRSE) onboard the US Shuttle SpaceLab [7], [8]. In 1994, two Shuttle Imaging Radar SIR-C/X-SAR missions were successfully flown in cooperation with NASA/Jet Propulsion Laboratory (JPL), USA [9], [10]. DLR and the Italian Space Agency (ASI) were responsible for the X-band radar instrument, while NASA/JPL was responsible for the fully polarimetric L- and C-band radar sensors. First multi-frequency repeat-pass SAR interferometric results were obtained [11].

The Shuttle Radar Topography Mission (SRTM) acquired in the year 2000 single-pass interferometric SAR data in X- and C-band by means of a 60-meter boom. This mission was also accomplished in cooperation with NASA/JPL, whereby DLR and ASI were responsible for the X-band interferometric radar system [12]. The SRTM mission provided a height accuracy in the order of 10 m at a posting of 30 m [13]. The coverage of the X-band DEM was limited to about 40% of the Earth surface, while the C-band radar from NASA/JPL had a coverage of 80% with a 10 m height error. Both DEM products were within −56° and +60° latitude.

Since 2007, TerraSAR-X, the first German SAR satellite, has been providing high resolution SAR images in stripmap, ScanSAR and sliding spotlight acquisition modes [14], [15],

[16]. Later on, a staring spotlight mode with an azimuth geometric resolution up to 25 cm has been implemented [17], [18]. A second almost identical X-band satellite was launched in 2010 and is flying since then in a close formation double helix orbit with TerraSAR-X [19], [20]. Both satellites form the TanDEM-X mission, which provided for the first time a global X-band DEM with a nominal height error of 2 m (point-to-point error, 90% confidence interval) at a horizontal posting of 12 m × 12 m. The global DEM data set is available since 2016 for commercial, scientific, and governmental applications. The data exploitation showed that users are very satisfied with the quality of the DEM dataset, which surpassed all the specifications in terms of absolute and relative accuracy as well as coverage [21].

Due to the excellent performance of TerraSAR-X and TanDEM-X, even being well beyond the nominal lifetime of 5.5 years, it was decided in 2017 to start with new global interferometric acquisitions. The aim is an updated global DEM and a DEM difference product, denoted as Change DEM [22], which is currently in processing.
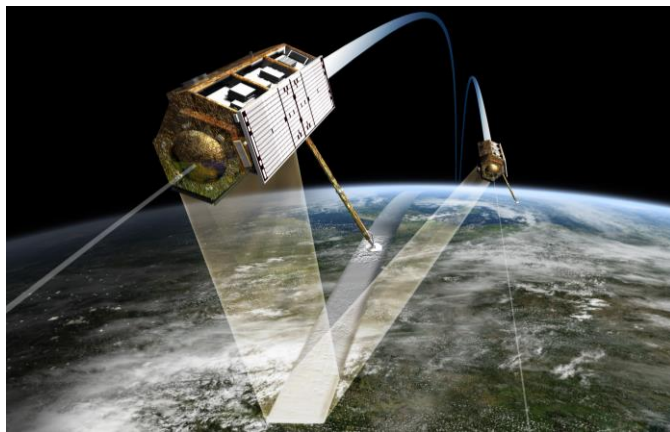

Fig. 1. Artist's view of TerraSAR-X and TanDEM-X, which are operating since 2007 and 2010, respectively, and build the first spaceborne interferometric SAR system consisting of two satellites in close formation flight. Both satellites are well beyond their design lifetime and are still producing interferometric data products of outstanding quality.

In order to keep the continuity of the TanDEM-X mission, several options for the realization of an interferometric mission have been analyzed as a follow-on of TanDEM-X. The DEM requirements were defined by a survey during the Phase 0/A of the HRWS study, involving the user community of TanDEM-X. A large demand was found for a global DEM with similar height accuracy but better horizontal posting (4 m × 4 m), in order to keep pace with the improved spatial resolution of spaceborne optical and SAR-image sensors. In addition, a release of an updated version of the DEM on a global scale, in order to cope with the dynamics of the topographic changes over the Earth's surface, was an important requirement. Last but not least, repeated interferometric acquisitions on a regional scale over areas with fast topographic changes (e.g., forests, ice sheets, megacities, infrastructure activity areas) as well as interferometric acquisitions on demand with a short DEM delivery time of weeks to months on a regional scale were also required by the user community.

The first analyzed concept was a bistatic configuration with two HRWS satellites, which has been discarded due to the high associated costs. Next, a concept with additional receive-only satellites has been analyzed as well. In order to cope with the aforementioned demanding user requirements, and to reduce the number of interferometric acquisitions while achieving the required DEM accuracy, it became evident that at least three receive-only satellites were necessary. Three receive-only satellites allow interferometric acquisitions with one small and one large baseline at the same time. However, the cost reduction was not significant due to the fact that each of the three receive-only satellites requires a complete receiver chain, data digitization and storage as well as downlink capability.

Finally, as an outcome of the system trade-off analysis, the MirrorSAR concept was identified and selected for the Phase A study of the HRWS mission as the only feasible solution, which allows for a low-cost implementation of an interferometric mission that fulfils the demanding user requirements in terms of accuracy, coverage, and timeliness.

Fig. 2 shows simulated DEMs that demonstrate the quality improvement expected from the HRWS-MirrorSAR mission. The simulation is based on data from DLR's airborne F-SAR sensor [49] obtained over Kaufbeuren in Germany. The methodology of the simulation is described in the Appendix. From top to bottom, the simulated DEMs show a) SRTM-/SIR-C with 30 m posting and 10 m height error, b) TanDEM-X with 12 m posting and 2 m height error, and c) HRWS-MirrorSAR with 4 m posting and 2 m height error. The height error is 90% point-to-point in all cases. The increased details of HRWS-MirrorSAR w.r.t. TanDEM-X are evident. Fig. 3 provides a zoom of the urban area within the black rectangle in Fig. 2.

Section II provides a general overview of the MirrorSAR concept as well as the details of the MirrorSAR add-on to HRWS. Section III estimates the SAR performance of the joint HRWS-MirrorSAR system as proposed for the DEM generation, while Section IV details on the baseline and orbit formation. In Section V, the echo window timing is discussed including a requirement on the allowed along-track separation between the HRWS satellite and the MirrorSAR satellite formation. The interplay between Doppler steering, satellite formation and MirrorLink is analyzed in Section V, too. The DEM height performance is derived in Section VI, where also an estimation of the DEM acquisition duration is provided. The details of the comparison of the simulated HRWS-MirrorSAR, TanDEM-X and SRTM DEMs are given in the Appendix.

II. MIRRORSAR

MirrorSAR is a concept that allows for low-cost Rx-only satellites within multistatic SAR multi-baseline formations without requiring complex SAR signal synchronization [23], [24], [25], [27], [28], [29].
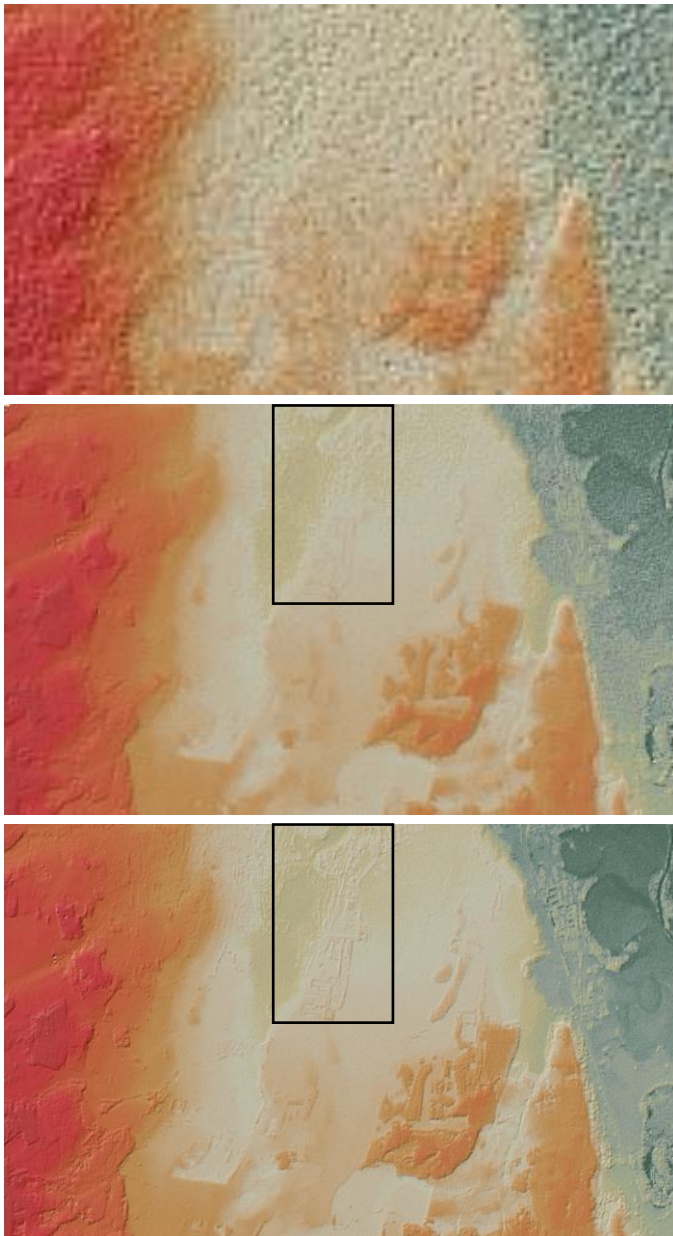
Fig. 2. From top to bottom: shade relief images of SRTM/SIR-C, TanDEM-X, and HRWS-MirrorSAR DEMs simulated from F-SAR X-band data.
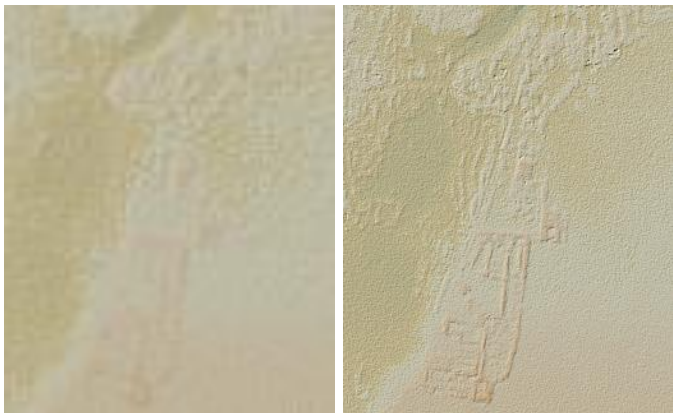

Fig. 3. (left) Zoom of the TanDEM-X DEM simulated from F-SAR X-band data over the urban area. (Right) The equivalent for the HRWS-MirrorSAR DEM.

The essential point of the multi-static MirrorSAR concept is the relocation of the radar receive antenna on-board a dedicated small radar receive-only satellite (Rx) while the radar receive chain comprising demodulation, digitization, data storage and downlink remains on-board the radar transmitting satellite (Tx). By doing so, the functionality of the Rx satellites is reduced down to space transponders only. This makes them simple, cheap, lightweight, and leads to a low-power supply. In the original MirrorSAR concept a dedicated Tx-only satellite provides the radar illumination.

For HRWS-MirrorSAR, this concept was adopted by exploiting the high transmit power, wide radar bandwidth, large memory, and high downlink capacity already provided by the monostatic HRWS satellite.

Another essential part of the MirrorSAR concept is the simultaneous acquisition of multiple large and small Rx baselines, which enables highly accurate and robust SAR interferometry. The helix orbit concept [36] has been proven to be reliable and safe by TanDEM-X [19]. The safety of the formation with respect to collision avoidance between the formation satellites is established by the separated maxima of cross-track and radial baselines at the equator and the poles, respectively, which means the avoidance of any orbit crossings. One possible MirrorSAR orbit formation is the extension of the helix orbit concept to nested helix orbits.

A. HRWS and MirrorSAR Satellite Parameter Assumptions

The assumed parameters for the design of the MirrorSAR complement are summarized in Table 1. The HRWS parameters are shown in the upper part of the table. The HRWS orbit is similar to the TerraSAR-X orbit. The radar frequency is X band.

Table 1: HRWS and MirrorSAR satellite parameters used in Phase A

HRWS	
TerraSAR-X orbit	514 km altitude, 11 day repeat cycle
radar frequency	9.8 GHz center, max. 1.2 GHz bandwidth
Tx average power	2.3 kW
Tx duty cycle	0.3
SAR antenna dimensions	6 m azimuth $\times$ 1.4 m elevation (8.4 m^2)
echo line recording	organized in PRIs
MirrorSAR satellites	
number of satellites	3
SAR antenna dimensions	3 m azimuth $\times$ 1.056 m elevation (3.2 m^2) (cf. Section III.B)
Rx bandwidth	200 MHz
noise figure+losses +margin	7.4 dB
SAR image resolution	1.5 m azimuth $\times$ 1.5 m ground range
sigma$_0$ model	Ulaby soil & rock, percentile 50 in coverage and ambiguous regions [30]
swath width	20 km ground range
swath overlap	1 km in ground range
incidence angle range	30° - 48.8° (full performance)
DEM height error	< 2 m (90%) point-to-point error at 4 m $\times$ 4 m horizontal posting

The echo recording is organized in echo lines with the maximum duration equal to the Pulse Repetition Interval (PRI). This reflects that HRWS is designed as a stand-alone monostatic SAR system that was only afterwards extended by MirrorSAR satellites. However, this design may be reworked in

the up-coming mission phases. The lower part of the table contains assumptions on the MirrorSAR add-on. Partly, these parameters have been obtained from optimizations during Phase A, but here they are introduced as assumptions in order to provide a more compact and clear paper. There are three MirrorSAR satellites with a radar bandwidth of 200 MHz each. Noise figure and losses are assumed to be quite high in consideration of the simple Rx-only satellites. Since the interferometric data are acquired in stripmap mode with a small swath width of 20 km, several elevation beams are required to cover the whole Earth with subsequent acquisitions. As the acquired swathes need to be mosaicked, sufficient overlap between adjacent swathes is required for interferometric calibration. A similar approach has been adopted for TanDEM-X with a swath width of 30 km.

B. MirrorSAR Add-on for HRWS

Fig. 4 illustrates the MirrorSAR acquisition geometry and radar signal flow. The HRWS satellite illuminates the ground area with its transmit radar beam in stripmap mode. The radar signal is backscattered from the ground surface and received by the three MirrorSAR satellites, which are arranged such that they form multiple baselines for single-pass cross-track interferometry. On-board the MirrorSAR satellites, the radar signal is up-converted to the MirrorLink frequency and, via the phase preserving MirrorLink it is passed to the HRWS satellite.

Since the received analog radar signal is available on board the HRWS satellite, the down conversion within the radar receive chain can be based on the same oscillator used for the generation of the radar transmit signal. Thus, the complex radar signal oscillator synchronization is avoided that usually goes along with classical bistatic SAR systems. Finally, the HRWS satellite downlinks the digitized radar signals to the ground station.

There are several options for the MirrorLink implementation [23], [24]. One possibility is to use a carrier frequency high enough to allow for amplitude modulation of the radar signal onto the link carrier. This requires only envelope detection on-board the Tx satellite and thus, completely overcomes the need to know the exact frequency/phase of local oscillators (LO) used on-board the MirrorSAR satellites.
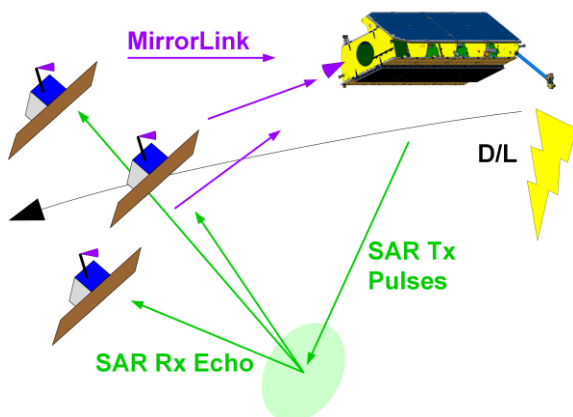

Fig. 4. MirrorSAR acquisition geometry of HRWS and three MirrorSAR satellites including the radar signal flow.
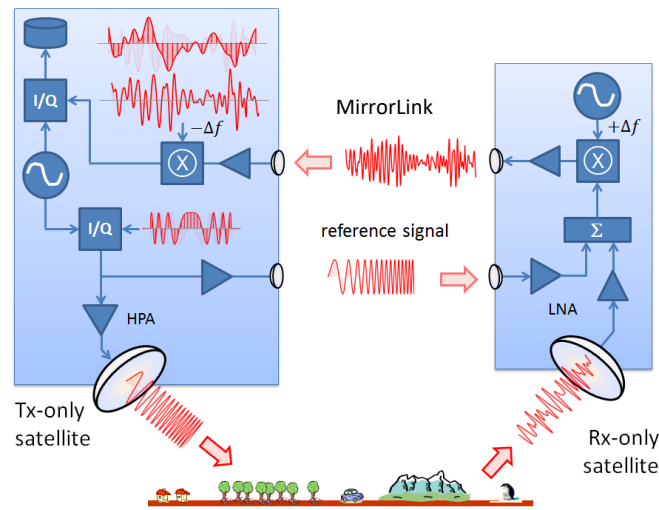

Fig. 5. Simplified synchronization by Double-MirrorLink.

For HRWS-MirrorSAR, the Double-MirrorLink [23], [24] was selected, whereby the radar signal is slightly shifted in frequency by Δf, as illustrated in Fig. 5. As the receiving bandwidth of HRWS is wide enough, the bands of the three MirrorLinks can be placed next to each other without further individual frequency conversion. Compared to, for example, TanDEM-X [19], the synchronization approach is simpler as no individual synchronization channel is required from the MirrorSAR satellites to the HRWS satellite. A simple reference signal is sent by using a low-gain link from HRWS to the MirrorSAR satellites, e.g., a copy of the radar pulses sent to the ground can be used. In addition to the measurement of the signal errors induced by the individual MirrorLink oscillators, the HRWS reference signal can also be used to determine small variations in the along-track distance between HRWS and a MirrorSAR satellite by measuring the reference signal's two-way delay. Moreover, internal delays, as e.g. introduced by the modulator on-board the MirrorSAR satellites, can be estimated as well.

The MirrorSAR satellites superimpose the reference signal to the radar echo. This addition overcomes the necessity to build another RF link between HRWS and the MirrorSAR satellite for the reference signal. After the superposition, the resulting signals are shifted by a frequency $+\Delta f$ using a coherent mixer. Then, they radiate the shifted signal back to HRWS, where the frequency shift is reversed before radar signal down-conversion. Any phase errors caused by MirrorLink up and down conversion based on the different LOs as well as from inter-satellite along-track distance variations are identical in the radar echo signal and in the double-mirrored reference signal, and can thus be corrected on-ground. The correction will be performed by measuring the time dependent amplitude and phase error of the double-mirror-linked reference signal. On-ground, this reference signal can be extracted with high fidelity by a narrow band Doppler filter, as the relative satellite velocities are almost constant. The double-mirror-linked reference signal can then be compared with an error-free reference signal that can be obtained from the internal calibration of the HRWS satellite. The estimated phase and amplitude errors are then corrected in the radar data.

The echo window timing discussion below analyzes a double MirrorLink synchronization with radar pulses as reference signal.

For HRWS-MirrorSAR, the helix orbit concept is extended to nested helix orbits. Each MirrorSAR satellite flies its helix around the HRWS orbit, which acts as a reference orbit. In Fig. 6 on the left, the yellow arrows indicate the largest and the smallest Rx cross-tack baseline.
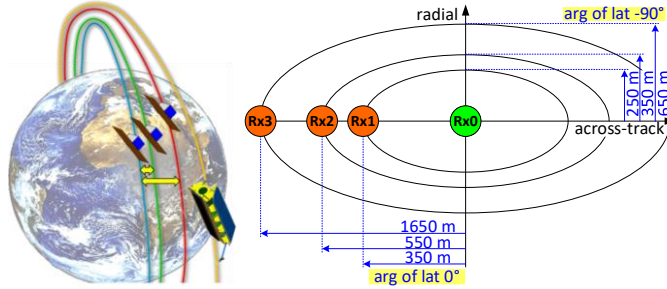

Fig. 6. (left) Nested helix orbits providing single-pass multiple Rx baselines. (right) Maximum cross-track and radial separations of the MirrorSAR satellites w.r.t. the HRWS reference orbit at the end of Phase A.

On the right in Fig. 6, the Phase A final baseline concept is shown. The maximum Rx baselines arise between Rx_1 and Rx_3; at the equator (0°/180° argument of latitude) in cross-track, and at the poles (±90°) in the radial direction. Rx_0 is only a virtual MirrorSAR satellite on the HRWS orbit that is about 15 km ahead of the HRWS satellite. The proposed HRWS-MirrorSAR orbit formation and baseline concept is further discussed in Section IV.

III. SAR Performance

There were two options considered to design the elevation beams for the SAR imaging, either to keep the ground swath widths constant, or to keep the elevation beam widths constant. In Phase A, for a better user convenience, a constant ground width was selected.

From the 20-km ground swath width with 1 km overlap in Table 1, and by considering an incidence angle range favorable for cross-track interferometry, 16 elevation beams were defined. Table 2 provides the incidence and look angles of the resulting beams. The total access range of beams 0 to 12 is above 240 km and provides a global coverage at the altitude of 514 km with incidence angles from 30° to 48.8°. The higher beams 13 to 15 are accepted to be less performant.

Table 2: Near and far incidence and look angles (i.e., $\theta_{i,near}$, $\theta_{i,far}$, $\theta_{lk,near}$, $\theta_{lk,far}$, respectively) for the elevation swaths with 20 km ground width and 1 km overlap. $\Delta\theta_{lk}$ is the beam width in look angle. All values in degree.

swath	0	1	2	3	4	5	6	7
$\theta_{i,near}$	30.0	31.8	33.4	35.1	36.7	38.2	39.7	41.1
$\theta_{i,far}$	31.8	33.5	35.2	36.8	38.3	39.8	41.2	42.6
$\theta_{lk,near}$	27.6	29.1	30.7	32.1	33.6	34.9	36.2	37.5
$\theta_{lk,far}$	29.2	30.7	32.2	33.6	35.0	36.3	37.6	38.8
$\Delta\theta_{lk}$	1.6	1.6	1.5	1.5	1.4	1.4	1.4	1.3

swath	8	9	10	11	12	13	14	15
$\theta_{i,near}$	42.5	43.8	45.1	46.4	47.6	48.7	49.8	50.9
$\theta_{i,far}$	43.9	45.2	46.4	47.6	48.8	49.9	51.0	52.0
$\theta_{lk,near}$	38.7	39.9	41.0	42.0	43.1	44.1	45.0	45.9
$\theta_{lk,far}$	39.9	41.0	42.1	43.1	44.1	45.1	46.0	46.8
$\Delta\theta_{lk}$	1.2	1.1	1.1	1.1	1.0	1.0	1.0	0.9

A. Geometric Resolution and Number of Looks

The single-look geometrical resolution in the SAR image was set to 1.5 m. After azimuth SAR processing with sidelobe suppression and antenna pattern compensation, the shape of the spectrum is assumed to be a generalized Hamming window with an α-coefficient of 0.6. In slant range dimension, no sidelobe suppression is assumed. The motivation for this choice is given in Section III.C.

From the resolution and the above described shape of the spectrum, a required azimuth bandwidth of 5480 Hz was derived. This bandwidth was one key input to the antenna pattern design described below. With an assumed oversampling factor of 1.13 the Pulse Repetition Frequency (PRF) is selected to be 6192 Hz. This value is used throughout all the performance calculations reported in this paper.

Due to the required geometric resolution of 1.5 m in the single look complex image and the chosen side lobe suppression strategy (cf. Section III.C), a radar signal bandwidth of 200 MHz was selected. The corresponding ground range resolution depends on the acquisition geometry and is shown in Fig. 7 versus incidence angle. For an interferogram with 1.5 m posting this makes range looks available. The number of range looks at swath center is indicated above the curve in red.
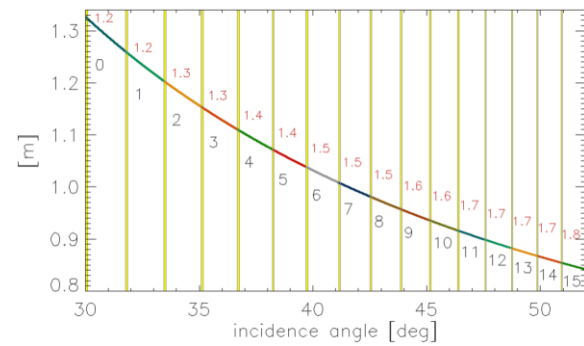

Fig. 7. SAR image ground range resolution versus incidence angle. Swath number below the curve. The number of range looks available for a ground resolution of 1.5 m at the swath centers is above the curve in red.

B. SAR Antennas and Pointing Error

Based on the Phase A HRWS antenna design and an assumed subarray structure and gain, several configurations of the Rx-only SAR antennas on-board the MirrorSAR satellites were analyzed, including phased array antennas with beam widening. The dimensions of the HRWS and the MirrorSAR phased array antennas, as finally defined for Phase A are as follows. The HRWS antenna has a dimension of 1.4 m in elevation and 6 m in azimuth, and the MirrorSAR antennas extend 1.056 m in elevation and 3 m in azimuth.

The antenna patterns are assumed to be separable into azimuth and elevation. Basic phase tapering has been applied to the HRWS pattern to widen the Tx beam in azimuth, and for the beams 0 to 4 also in elevation. The antenna patterns as described below are the result of a few iterations w.r.t. the SAR performance. There is, however, still potential for improvement in upcoming mission phases.

The HRWS transmit azimuth pattern as cut through a two-dimensional antenna pattern without elevation phase tapering

(e.g. elevation beam 12 in Fig. 9 on the right) is shown in Fig. 8 on the left in green color. The reduction of the Tx gain due to the beam widening is 0.53 dB. The MirrorSAR Rx azimuth pattern is without any tapering and shown in red color. The resulting two-way azimuth pattern is depicted in black color, and the yellow angle span corresponds to the azimuth bandwidth that needs to be processed to achieve an azimuth resolution of 1.5 m.
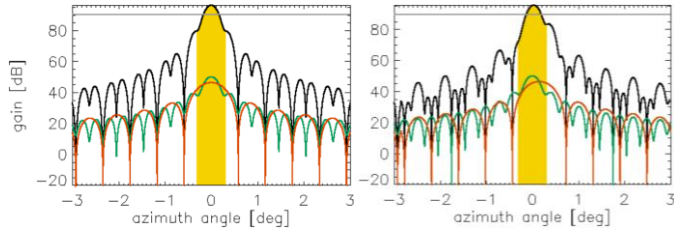

Fig. 8. Two-way azimuth patterns (black). HRWS (Tx, phase tapering, green), Mirror (Rx, red), azimuth angle width for 1.5 m azimuth resolution (yellow span). Horizontal line indicates 6 dB beamwidth of two-way pattern. (left) No pointing error. (right) Perfect pointing of 0° error for HRWS and 0.15° pointing error for MirrorSAR satellites.

In order to reduce the cost for the MirrorSAR satellites, a weaker requirement on the pointing accuracy is desirable. Thus, the SAR and DEM performance below is calculated for a varying pointing error. The pointing error is introduced by a mis-pointing of only the MirrorSAR pattern in azimuth and elevation. The HRWS pointing is assumed to be much more precise than the pointing of the low-cost MirrorSAR satellites. The influence of the HRWS pointing error is thus neglected in the performance estimation, which means to set it to 0° pointing error. Fig. 8 shows on the right the azimuth pattern for 0.15° MirrorSAR pointing error.

Fig. 9 shows elevation patterns. On the left for beam 0, the HRWS Tx, the MirrorSAR Rx and the two-way pattern are shown for 0° pointing error. On the right for beam 12, the patterns are shown for 0.15° pointing error. The maxima of the two-way patterns equal the two-way gains, i.e., the maximum of the two-dimensional two-way pattern. In the plots, the gain is not considering the loss due to azimuth beam widening. The yellow look angle span indicates the 20 km ground swath width.
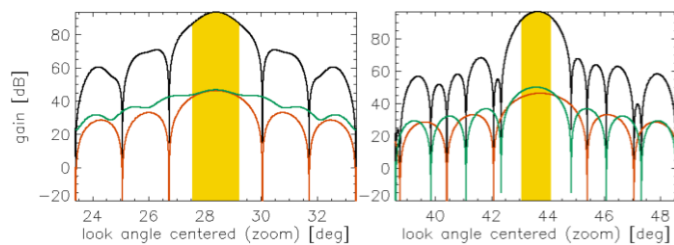

Fig. 9. Elevation patterns versus look angle with maxima equal to the maximum of the two-dimensional pattern. HRWS (Tx, green), Mirror (Rx, red), two-way (black), and look angle span corresponding to 20 km swath width (yellow). (left) Elevation beam 0 with Tx elevation phase tapering. No pointing error. (right) Elevation beam 12 w/o any tapering. Pointing error of 0.15° in MirrorSAR pattern and HRWS pointing w/o error.

A detailed analysis of the required pointing knowledge was not performed in Phase A as it has only a very small effect on the interferometric phase and can be determined with sufficient accuracy in the on-ground post processing by evaluating both the star sensor and the SAR data.

C. Noise Equivalent Sigma Zero (NESZ)

The details below were considered in the NESZ calculation.

Antenna Pattern and Gain. Antenna pattern widening is made only through Tx phase settings, which means no change in the Tx peak power. The 2-dimensional pattern is approximated by azimuth and elevation pattern cuts.

Sidelobe Suppression in the SAR processing. In range, no sidelobe suppression is performed and the better geometric resolution is exploited to obtain more interferometric looks.

The azimuth antenna pattern introduces an *Inherent Weighting* (IW) of the azimuth spectrum that, if not corrected for, acts like a sidelobe suppression. This inherent weighting should not be corrected in order not to amplify the noise. This has the effect of an *inherent* sidelobe suppression on the azimuth impulse response function (IRF) that depends only on the shape of the azimuth pattern. An approximation to this inherent sidelobe suppression is to correct for the antenna pattern and to perform a spectral weighting that is close to the azimuth pattern itself. This has the advantage of a defined shape of the azimuth Impulse Response Function (IRF) that allows for controlled performance parameters including geometric resolution and peak-to-sidelobe ratio, while the noise amplification is kept small. This Approximated Inherent Weighting (AIW) is applied in the following.

For the HRWS-MirrorSAR system designed above, a Hamming weighting $H_W(f_a)$ is defined along the azimuth frequency f_a over the processed azimuth bandwidth B_a with an α-coefficient of 0.6, which turned out to be close to the normalized amplitude of the two-way azimuth pattern $P_{az,amp,norm}$. The relative effect of the approximated inherent sidelobe suppression on the azimuth signal and noise spectra can be observed in Fig. 10, and is briefly discussed as follows. The discussion is based on the NESZ terms in (1)

$$NESZ_{NW} = \frac{c_{NESZ}}{G_{P,2D,max} \cdot G_{C,rg} \cdot G_{C,az}} \cdot \frac{\int\limits_{B_{az}} 1^2 \, df_a}{\int\limits_{B_{az}} \left[P_{az,amp,norm}\left(f_a\right) \right]^2 df_a}$$

$$NESZ_{ANW} = \frac{c_{NESZ}}{G_{P,2D,max} \cdot G_{C,rg} \cdot G_{C,az}} \cdot \frac{\int\limits_{B_{az}} 1^2 \, df_a}{\int\limits_{B_{az}} \left[H_W\left(f_a\right) \right]^2 df} \cdot \frac{\int\limits_{B_{az}} \left[\frac{H_W\left(f_a\right)}{P_{az,amp,norm}\left(f_a\right)} \right]^2 df_a}{\int\limits_{B_{az}} 1^2 \, df_a} \tag{1}$$

where $G_{P,2D,max}$ is the gain of the elevation pattern as cut through the 2-dimensional pattern at the gain maximum (cf. Fig. 9). $G_{C,rg}$ and $G_{C,az}$ are the correlation gains in range and azimuth, respectively, that follow from the corresponding time-bandwidth-products. c_{NESZ} is a constant that contains other standard NEZS contributions. The first line refers to IW by the azimuth pattern. Since $G_{C,az}$ is derived for a constant azimuth spectrum amplitude, the signal power reduces due to the antenna pattern as is expressed by the second fraction. For the system under discussion, the signal power reduction is 4 dB. The IW has no impact on the noise power as no manipulation of the azimuth spectrum applies. Fig. 10 provides in the green and red solid lines the normalized amplitude of the signal and noise spectra, respectively, for IW. The green amplitude spectrum is equivalent to the normalized pattern. The red amplitude reflects the constant amplitude of the noise spectrum.

The second line of (1) is for AIW and the resulting shape of the signal and noise amplitude spectra are shown in Fig. 10 by the dashed curves. The resulting shape of the amplitude spectrum after AIW is $H_W(f_a)$, and the reduction due to the not constant azimuth spectrum given by the second fraction in (1) is here 3.6 dB. A better value as for IW but the noise power is increased w.r.t. IW, too. The noise power increase resulting from the third fraction due to noise spectrum weighting is 1.4 dB. In summary, the change from IW to AIW for the system under discussion resulted in a signal power increase of 0.4 dB, a noise power increase of 1.4 dB, and thus a NESZ deterioration of 1 dB.
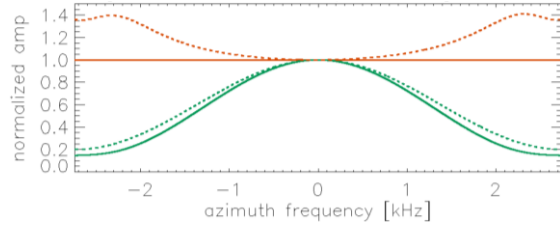

Fig. 10. Effect of approximated inherent weighting (AIW) for sidelobe suppression on signal and noise spectra during compression. (solid) Signal spectrum in green color with inherent weighting from antenna pattern amplitude and uniformly distributed noise spectrum in red color. (dashed) Spectra of signal and noise after applying approximated inherent weighting.

Considering the above-mentioned details, a standard NESZ calculation results in the NESZ performance in Fig. 11.
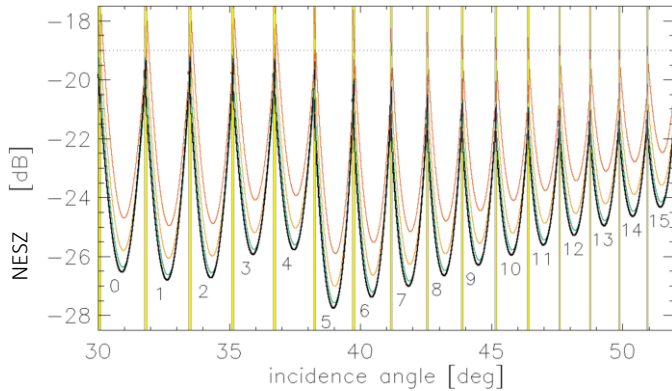

Fig. 11. NESZ for the incidence angle range of the 16 elevation beams. The beam overlap of 1 km ground range is represented by the small yellow vertical areas. The thick black NESZ curves are for 0° pointing error. The smaller lines in green, orange and red color are the NESZ curves for 0.05°, 0.10° and 0.15° pointing error, respectively.

The performance is shown for pointing accuracies of 0°, 0.05°, 0.1°, and 0.15°. Taking into account the overlap areas, the worst NESZ for 0° pointing error is -21.3 dB and deteriorates to -17.8 dB for 0.15° pointing error.

D. Ambiguity Ratios

The Azimuth Ambiguity-to-Signal Ratio (AASR) derives from the azimuth antenna pattern, the processed azimuth bandwidth, the applied sidelobe suppression weighting, the PRF and the pointing error. It is constant for all elevation swaths and is equal to -20.4 dB for 0° pointing error. The ratio degrades for 0.05°, 0.10°, and 0.15° pointing errors to -18.7 dB, -15.2 dB, and -10.7 dB, respectively.

The Range Ambiguity-to-Signal Ratio (RASR) depends on the acquisition geometry, the PRF, and strongly on the shape of

the elevation antenna pattern. Applying Ulaby [30] soil & rock with percentile 50 for the swath coverage and ambiguous regions results in the RASR in Fig. 12.
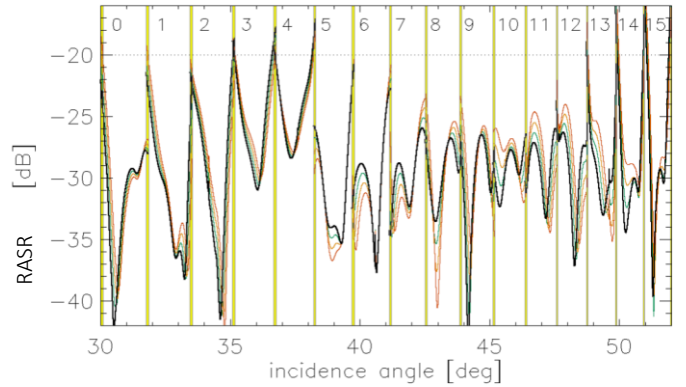

Fig. 12. RASR versus incidence angle. The thick black curves are for 0° pointing error. The smaller lines in green, orange and red color are the RASR curves for a pointing error of 0.05°, 0.10° and 0.15°, respectively.

E. Pointing Accuracy Specification

Table 3 summarizes the performance and its degradation for increased MirrorSAR satellite pointing errors for the swaths/elevation beams 0 to 12 that are required for global coverage. The pointing error has been simulated by introducing appropriate pointing offsets of the Rx azimuth and elevation patterns, as described above. The table provides the worst values found from all incidence angles in beams 0 to 12.

Table 3: Summary of SAR performance in the beams 0 to 12 for different MirrorSAR pointing errors.

Mirror pointing error	0.00°	0.05°	0.10°	0.15°
NESZ	-21.3 dB	-20.5 dB	-19.6 dB	-17.8 dB
RASR (worst of all beams)	-17.0 dB	-17.2 dB	-17.7 dB	-18.0 dB
AASR	-20.4 dB	-18.7 dB	-15.2 dB	-10.7 dB

The Rx pointing error deteriorates the AASR, RASR, and NESZ, and this propagates into the interferometric error. In Phase A, meaningful criteria for SAR image generation were applied, as they were for TerraSAR-X [31]. The AASR performance shows the strongest deterioration and based on the SAR image performance results, the Phase A Rx MirrorSAR pointing error is specified to be not larger than 0.05°.

Further improvement of the ambiguity and NESZ performance can be expected by advanced antenna pattern design. Also, advanced techniques for ambiguity suppression should be considered. Frequency selective ambiguity suppression techniques can be applied especially in case of pointing errors [43], [44].

IV. BASELINE AND ORBIT FORMATION

While the baseline design will be refined in the next mission phases, in Phase A a preliminary set of baselines has been selected based on the following considerations.

- The driving point for the baseline design is the required vertical accuracy of the DEM. The DEM height accuracy is directly related to the Height of Ambiguity (HoA) and therefore to the baseline length [19],[45].
- For flat terrain, soil and rock and low vegetation terrain surface, the maximum HoA should be around 20 m at the

equator up to an incidence angle of 50°. This is comparable to high-resolution DEMs in the TanDEM-X mission [46]. Thus, the largest cross-track baseline between Rx_1 and Rx_3 was derived to be 1300 m at the equator.

- For acquisitions over forests or mountainous terrain, HoA values in the order of 30 m - 50 m are required in order to mitigate decorrelation effects [47]. This could be realized by using in addition acquisitions from Rx_2.

- For phase unwrapping an additional smaller baseline is furthermore required [48]. Considering a safe orbit formation, the small cross-track baseline was set to 200 m between Rx_1 and Rx_2. Alternatively, two baselines with a fixed ratio (around 0.7) could be used similar to the TanDEM-X approach. This trade needs to be further assessed in the next mission phases.

- The resulting cross-track baseline between Rx_2 and Rx_3 is 1100 m and is close to the large cross-track baseline of 1300 m. This provides more acquisition flexibility.

A straight-forward nested helix orbit formation would achieve the large Rx baseline by two MirrorSAR satellites with symmetric cross-track baselines of ±650 m w.r.t. the reference HRWS orbit. The next subsection discusses the drawback of this concept.

A. MirrorLink, Formation Geometry and Doppler Steering

Basically, the MirrorLinks need to be oriented along the satellites' flight direction. A reasonable assumption for low-cost MirrorSAR satellites is the use of non-steerable MirrorLink antennas. One major driver in their design is the required beamwidth. Fig. 13 shows the formation geometry in the along-/across-track plane that is most relevant for the horizontal beamwidth.

The horizontal beamwidth needs to cover the relative formation position of the Tx HRWS and the Rx MirrorSAR satellites shown on the right of Fig. 13. At the equator, the Rx baselines are maximum in the across- and along-track directions. The Doppler steering yaw angle is also maximum at the equator and thus the maximum required horizontal beamwidth arises at the equator.
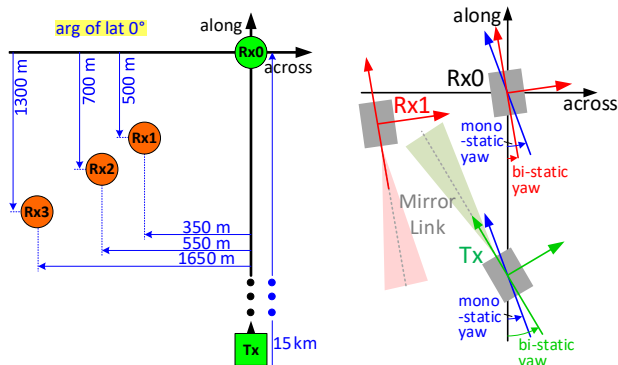

Fig. 13. (left) Maximum along- and across-track baselines at the equator. Together with Fig. 6 on the right, the illustration shows the baselines defined at the end of Phase A. (right) MirrorLink pointing direction in along/across-plane. The yaw angle from the Doppler steering rotates the Tx and Rx pointing into opposing directions. Additionally, the yaw needs to consider the bistatic acquisition and thus rotates further towards forward/backward steering w.r.t. a monostatic yaw steering that is colored in blue. The horizontal MirrorLink beamwidth is indicated in light red and light green colors.

In Phase A, the Doppler steering was approximated by a monostatic Total Zero Doppler Steering (TZDS) [34] and an additional forward/backward steering via the yaw angle required for the bistatic acquisition.

One significant finding is that due to the Doppler steering, all MirrorSAR satellites need to be positioned on the same side of the HRWS orbital plane. Looking to Fig. 13 (left), it is clear that a positioning of, e.g., Rx_3 on the opposite side of Rx_1 would significantly increase the required beamwidth.

The quantitative effect of selecting the proper side of the orbit plane for the MirrorSAR satellites can be observed in Fig. 14. The red curve shows in both plots the required MirrorLink beamwidth for HRWS and Rx_0, which is only virtual and exactly on the HRWS orbit plane. Thus, it reflects the contribution of the bistatic yaw angle that varies along the orbit. The continuous and dashed line styles are for 30° and 48.8° of incidence angle, respectively. The monostatic TZDS is not dependent on the incidence angle [34], but the additional forward/backward angle for the bistatic acquisition is.
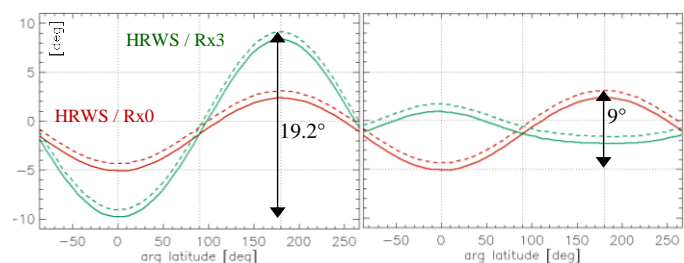

Fig. 14. Required horizontal MirrorLink beamwidth for HRWS/Rx_0 (red, only virtual) and HRWS/Rx_3 (green) in solid line style for 30° incidence angle and dashed line style for 48.8°. Y-axes in degree. (left) Yaw steering rotates the MirrorLink pointing away from the formation. (right) Yaw steering rotates into the formation.

The curves in Fig. 14 show the maximum required angles off the along-track direction in the along-track/cross-track plane, which result from the formation geometry and the Doppler steering. The beamwidth of the MirrorLink needs to cover all these angles. In the left plot, the MirrorSAR satellites are on the unfavorable side of the HRWS orbital plane, where the yaw angle rotates the MirrorLink pointing away from the formation. The required MirrorLink horizontal beamwidth would be 19.2°. In the right plot, the MirrorSAR satellites are on the favorable side and the beamwidth is minimized to 9°.

The approach above was also applied to derive the required vertical beamwidth in the along-track/radial-plane. The pitch angle is much smaller than the yaw in TZDS (< 0.1° for a TerraSAR-X orbit) and the counterbalancing effect is much smaller. A required vertical beamwidth of 5° was estimated.

B. Resulting Baselines and HoA

As discussed in the previous section, another consideration is thus added to the baseline design:

- All MirrorSAR satellites shall be on the side of the HRWS orbit plane to which the Doppler steering yaw angle rotates the MirrorLink antenna pointing of the HRWS satellite.

Following all considerations, the Rx orbital formation was optimized and the resulting one is shown with its maximum

baselines in Fig. 6 (right) and Fig. 13 (left). The maximum Rx baselines result from the MirrorSAR satellites Rx_3 and Rx_1, the minimum baselines from Rx_2 and Rx_1. Fig. 15 shows in the left plot these baselines along the orbit as a function of argument of latitude. The horizontal lines indicate the maxima of the across- and along-track baselines at the equator as well as the maxima of the radial baselines at the poles that are defined in Fig. 6 (right) and Fig. 13 (left). The baseline curves in Fig. 15 on the left are in Earth-fixed geometry as needed for SAR interferometry. The baseline curves in inertial geometry fit exactly in-between the baseline maxima. In Earth-fixed representation, an inherent offset in the cross-track baselines is visible, which is caused by the Earth rotation. For the larger Rx_3/Rx_1 baseline the offset is 50 m at the maxima.

The right plots in Fig. 15 provide the corresponding Height of Ambiguity (HoA). The plot on top shows the HoA for ascending and descending orbits versus the target latitude on ground. The HoA curves are represented for the minimum, mean, and maximum incidence angle (red, blue, green curves in the figure) that is covered by swaths 0 to 15.
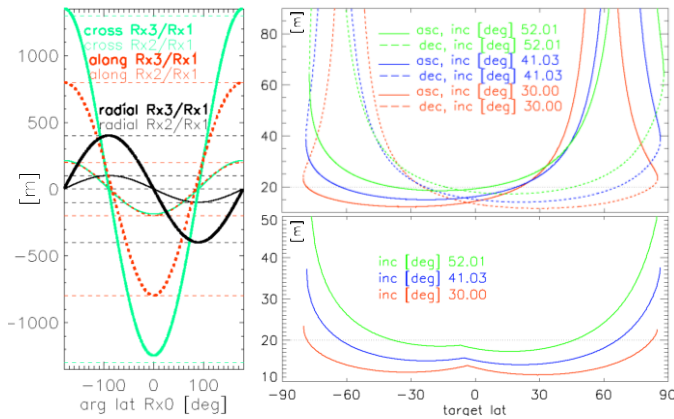

Fig. 15. (left) Maximum and minimum Rx baselines of the MirrorSAR satellite Rx formation along the orbit in Earth-fixed geometry. (right) HoA of the larger Rx baseline for the minimum, mean and maximum incidence angle covered by the swaths 0 to 15 versus target latitude. (top) For ascending and descending orbits. (bottom) The smallest HoA selected from ascending and descending orbits.

The plot on the bottom provides the minimum HoA resulting from ascending and descending orbit curves versus ground target latitude. As desired, the maximum HoA at the equator is below 20 m for 50° incidence angle.

V. ECHO WINDOW TIMING

With respect to classical monostatic echo window timing calculation that provides adequate PRFs based on diamond diagrams, the following considerations are required [27]:

- The nadir echoes need to be specified more generally for the bistatic operations.
- The signal path along the MirrorLink generates additional delays.
- The positions of all MirrorSAR satellites in the Rx formation need to be included.
- The organization of the Echo Receiving Window (ERW) recording on-board the HRWS satellite is to be considered. In

Phase A, the assumption was made that it is organized in PRIs, which implies that the maximum echo window length is given by the PRI.

- The assumed HRWS recording based on PRI intervals imposes restrictions on the allowed along-track separation between HRWS and the MirrorSAR satellite formation.
- The transmit interferences do not reduce the swath width, as the HRWS satellite can transmit and receive via the MirrorLink at the same time. This unusual feature becomes possible by combining the bistatic MirrorSAR acquisition geometry with the frequency shift within each receiver before forwarding the radar echo data with the MirrorLink.

A. Nadir and Forward Reflection Area

In the monostatic case, the nadir area around the satellite's nadir point contains the strongest non-swath ground reflections that interfere with the echo signal from the desired swath. The nadir area can be defined by a nadir angle θ_N that is rotational symmetric around the nadir direction. From TerraSAR-X experience, a reasonable X-band value for θ_N is 1.5° [33]. In the bistatic acquisition case, which applies for HRWS-MirrorSAR, we define a Forward Reflection Area (FRA) that contains the strongest (direct) reflections outside the desired swath. Fig. 16 shows this area as an ellipse below the Phase Center (PC) resulting from the Tx HRWS and Rx MirrorSAR satellite antenna positions, which are separated by the along-track separation D_{RT} in the figure.

In the timing calculations below, the FRA was approximated by a simple rectangle whose edges are the four blue points in the figure. In cross-track, the points are at ±1.5° look angle, and are thus assumed to be as large as θ_N in TerraSAR-X. The slant ranges r_0 are defined from the PC position in boresight geometry.
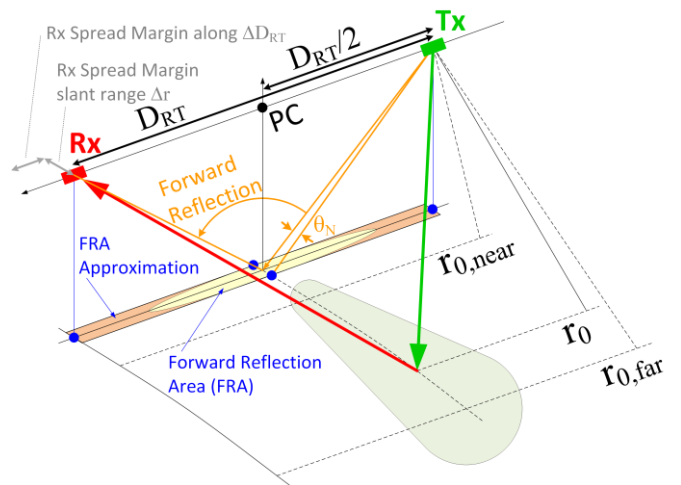

Fig. 16. Forward reflection area in bistatic acquisition geometry, which contains the strongest echoes outside the illuminated swath. The Rx spread margins in along-track and Rx path length cover the different positions of the three MirrorSAR satellites within the Rx formation.

B. MirrorSAR Diamond Diagram

The window timing regulates the temporal positioning of the Tx pulses sent to ground and towards the MirrorSAR satellites, and the FRA echoes. The following additional rules and assumptions are made [27]:

- Spherical Earth model and symmetric swath position as is shown in Fig. 16. Range cell migration margin neglected, guard times and internal delays neglected.
- Simultaneous transmission of Tx pulses from HRWS to ground and to Rx MirrorSAR satellites.
- Tx pulses can overlap with ERW (isolation by spatial separation of HRWS and Rx MirrorSAR satellites) as well as with the double-mirrored Tx pulses (isolation by different carriers in synchronization forward and MirrorLink back channels).
- FRA echoes can overlap with Tx pulses in the synchronization fore channel (isolation by directivity) and the MirrorLink back channel (isolation by different carriers).
- FRA echoes cannot overlap with ERW, but can overlap with the receiving window pulse extension (FRA echoes do not saturate receivers).
- Receiving window including extension cannot exceed a single PRI from Tx pulse rising edge to next pulse rising edge. The same restriction holds for the double-mirrored Tx synchronization pulses.
- The Rx formation of the MirrorSAR satellites is modelled by a slant range margin Δr that prolongs the receive path of the closest MirrorSAR satellite by 1 km, and by an along-track margin ΔD_{RT} that prolongs D_{RT} between HRWS and the closest MirrorSAR satellite (cf. Fig. 16) by 2 km. The FRA is not modified by these margins (approximation). Δr prolongs the focused ERW. ΔD_{RT} extends the delay of the synchronization Tx pulses.

Fig. 17 shows the diamond diagram for an along-track separation D_{RT} of 13 km between HRWS and the closest MirrorSAR satellite. The echo window timing assures the recording of all the SAR signals received from the three MirrorSAR satellites in the Rx formation by means of the formation spread margins in slant and along ΔD_{RT} and Δr, respectively, that were introduced in Fig. 16. The Tx pulses transmitted to ground and to the MirrorSAR satellites are depicted in yellow. The start and end times of the blue Focused Echo Window (FEW) correspond to the related beams near and far incidence angles, respectively. These start and end times include the full signal path from HRWS to ground, from ground to the MirrorSAR satellite, and from the MirrorSAR satellite to HRWS. Δr converts into the solid addition on the right of the FEW. The usual pulse length extension in red completes the FEW to the longer ERW. Due to the bistatic acquisition and the frequency shift, the Tx pulses can overlap with the ERW. Limitations to the ERW are imposed by the FRA echoes in gray color that cannot overlap with the FEW, and by the recording within a single PRI restriction.

The synchronization Tx pulses returned from the MirrorSAR satellites to HRWS via the MirrorLink are drawn in green. ΔD_{RT} extends these pulses by the part in orange. In Section III.A, the PRF was set to 6.2 kHz. This is drawn in the figure by the black horizontal line. Above, the swath number is tagged. The swaths 0 to 12 can be acquired by PRFs from 5.8 to 6.45 kHz as is indicated by the dashed horizontal lines.
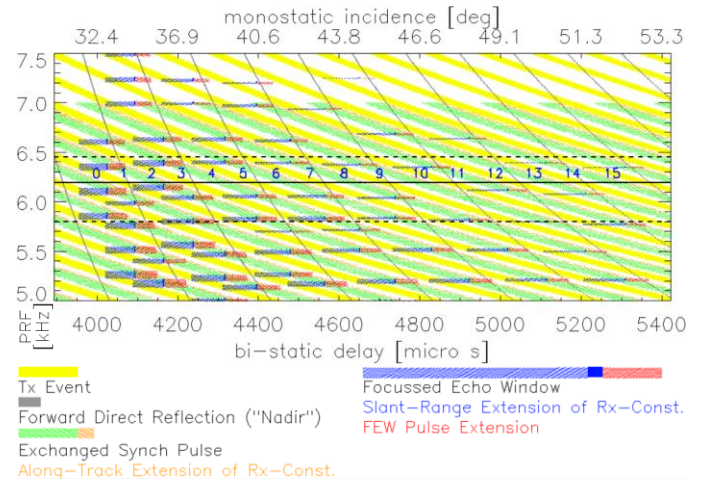

Fig. 17. Diamond diagram for bistatic HRWS MirrorSAR. Bottom axis is the overall bistatic delay time. Top axis is equivalent to the boreside incidence angle from the phase center PC and is denoted by *monostatic* incidence angle.

C. Along-Track Separation HRWS - Rx Mirror Formation

In Fig. 17, there is an area above the PRF value of 7 kHz where no more exchanged synchronization Tx pulses are plotted (green and along-track extension in orange). This is caused by the limitation of an echo line to be smaller than one PRI. For the along-track separation D_{RT} of 13 km and PRF values above 7 kHz, the PRI borders would be violated.

The allowed along-track separations D_{RT} between HRWS and the closest MirrorSAR satellite as a function of the PRF can be derived from Fig. 18 [27]. The allowed minimal and maximal separations depend on the number of travelling pulses n_{trav} along the MirrorLink:

$$D_{RT,\min}\left(n_{trav}\right) = \frac{n_{trav}}{PRF} \cdot \frac{c_0}{2}$$

$$D_{RT,\max}\left(n_{trav}\right) = \left(\frac{n_{trav}+1}{PRF} - \frac{duty}{PRF}\right) \cdot \frac{c_0}{2} - \Delta D_{RT} \quad (2)$$

where *duty* is the Tx duty cycle. Starting at the rising edge of a Tx pulse, the minimum $D_{RT,min}$ corresponds directly to the rising edge of a Tx pulse. Remember the above assumption that the returned synchronization pulses are allowed to interfere temporally with the Tx pulses of HRWS. The associated maximum $D_{RT,max}$ is calculated by subtracting the pulse length $T_p = duty/PRF$ and the along-track extension of the Rx constellation $\Delta D_{RT} \cdot 2/c_0$ from the PRI that starts at the selected Tx pulse. The symbol for the speed of light is c_0.
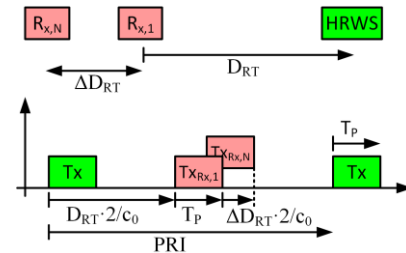

Fig. 18 Along-track separation D_{RT} and limitation to one PRI.

Based on the above calculations and assumptions, the relation between PRF and the allowed separations between HRWS and the closest MirrorSAR satellite D_{RT} is provided in Fig. 19. The green zones show allowed combinations; the red zones combinations that are not possible.
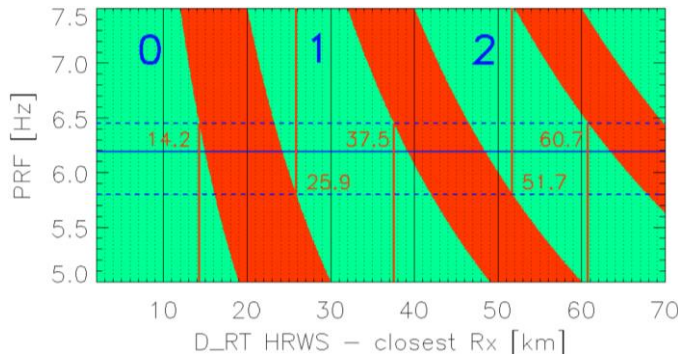
Fig. 19. Allowed along-track separations between HRWS and the closest MirrorSAR satellite versus PRF.

The number of travelling pulses along the Double MirrorLink is indicated in the green zones by a blue number. From the required PRF band that is obtained from the diamond diagram and that is within the dashed blue lines in the figure, the minimum and maximum along track separations derive. For example, in case of one travelling pulse, the along track separation between HRWS and the closest MirrorSAR satellite is allowed to be within 25.9 and 37.5 km.

VI. DEM HEIGHT PERFORMANCE

In the beginning of this section, the trade-off that resulted in the number of three MirrorSAR satellites is discussed. The ensuing height error estimation follows in large parts the approach used for TanDEM-X [19]. The SAR performances NESZ, AASR, and RASR are taken from above for the MirrorSAR satellite pointing accuracy of 0.05°, and are assumed to be equal in both interferometric channels.

The interferometric phase error and associated height error estimation in this section is considering only the largest Rx baseline. Theoretically, the other Rx baselines, but especially the second larger baseline with 1100 m in cross-track at the equator, could be exploited to decrease the interferometric phase error, e.g. [34]. However, the 3 available Rx baselines provided by the 3 MirrorSAR satellites are not totally independent from each other since the phase error in the signal of one MirrorSAR satellite is the same in the two baselines it is used for. This is currently a topic of research but in the scope of Phase A we decided to apply a conservative approach and derived the interferometric phase error from the largest Rx baseline only. Note, for TanDEM-X the two baselines are formed by means of repeat-pass acquisitions and are thus completely independent. Consequently, the interferometric phase error estimation considers the decrease of the phase error provided by the second baseline (cf. Section III.C in [19]).

A. MirrorSAR Satellite Number and Single-Pass Baselines

The decision to design the Rx formation with three satellites is a result of the trade-off between general improvement in acquisition time, DEM height sensitivity, phase unwrapping accuracy, and the overall mission cost that obviously rises with the number of MirrorSAR satellites.

Based on the experience with TanDEM-X, at least two baselines are required to achieve a high-quality DEM, i.e., a large baseline to provide a high sensitivity to the elevation height, and a small baseline to achieve a stable phase-

unwrapping. TanDEM-X acquires only one baseline per pass and thus requires two repeated passes over the same region of interest. Likewise, HRWS with two MirrorSAR satellites provides only one (Rx) baseline per pass.

An increase to three MirrorSAR satellites offers three Rx baselines per pass. First, this is a great improvement in terms of DEM acquisition time. Second, the three baselines are acquired simultaneously and thus, temporal decorrelation is eliminated. For example, phase unwrapping is more difficult in case that the two baselines are not acquired at the same time due to, e.g., different depth of penetration in forested areas. A quantitative prediction of the phase unwrapping improvement when comparing two MirrorSAR satellites with three ones is difficult but TanDEM-X experience [46] clearly favored three MirrorSAR satellites.

An increase to four MirrorSAR satellites was not further considered in Phase A mainly due to cost reasons. Another consideration was the increase in total MirrorLink bandwidth for all Rx satellites and the associated increase of data volume caused by a fourth MirrorSAR satellite.

B. Total Coherence

One basic step is the calculation of the total coherence γ_{tot}:

$$\gamma_{tot} = \gamma_{SNR} \cdot \gamma_{AMB} \cdot \gamma_{QUANT} \cdot \gamma_{RG} \cdot \gamma_{AZ} \cdot \gamma_{VOL} \qquad (3)$$

As is done in the single-pass system TanDEM-X, no temporal decorrelation is considered. With respect to volume scattering, the performance analysis focuses on surface areas and assumes a predominant surface scattering with only a small residual volume decorrelation [47]. Thus, a high value for γ_{VOL} is assumed, i.e., 0.985.

The coherence value $\gamma_{RG} = 0.984$ for range mis-registration is taken from TanDEM-X as well as the high coherence value $\gamma_{AZ} = 0.989$ for azimuth spectrum non-overlap decorrelation that assumes independent TZDS of both satellites [19].

In Fig. 22 (a) of [32] it is shown that for the HRWS-MirrorSAR geometry a steering to zero Doppler or constant Doppler of all three bi-static images can be obtained if an azimuth displacement of the Rx beams w.r.t. the Tx beam is allowed. The azimuth displacement is worst at the equator with an estimated displacement of 1200 m. In the TanDEM-X case [19], the azimuth displacement was 1000 m. As the Rx beam azimuth displacements as well as the orbits are similar, in Phase A the pointing strategy of TanDEM-X was selected, too, i.e. to achieve an almost perfect azimuth spectrum overlap and to allow a small Rx azimuth pattern displacement. Accordingly, the azimuth correlation value of 0.989 due to azimuth spectra non-overlap was used in the coherence calculation. In the coming mission phase, a more detailed trade-off between azimuth Rx pattern displacement and azimuth spectra non-overlap will be carried out considering the improved Doppler steering methods in case of multi-static acquisitions [32].

A 4-bit quantization is assumed, and the corresponding coherence value $\gamma_{QUANT} = 0.989$ is also taken from [19]. In many systems, the decorrelation due to the Signal-to-Noise Ratio (SNR) is the largest one. The corresponding correlation coefficient γ_{SNR} is calculated assuming equal SNR in both interferometric channels [37]:

$$\gamma_{SNR} = \frac{1}{1 + SNR^{-1}} \tag{4}$$

The SNR is obtained by subtracting the NESZ for 0.05° pointing error from the σ_0 value, both in dB. The backscatter coefficient σ_0 is taken from Ulaby [30] for soil and rock in HH polarization with a percentile of 90. Fig. 20 shows the input to the SNR calculation.
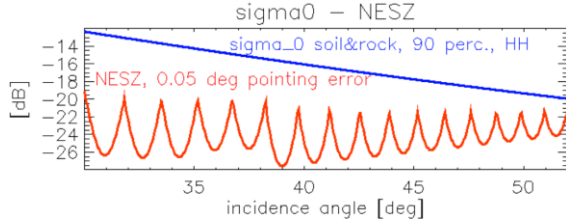

Fig. 20. Input to SNR calculation, σ_0 (sigma_0) and NESZ.

Following [19], the coherence γ_{AMB} related to the distributed range and azimuth ambiguities is approximated by considering the ambiguities as pure noise, which means to assume incoherent ambiguities. However, for some orbit configurations coherent azimuth ambiguities might determine more severe degradation in the interferograms [40], [41], [42]. With the above assumption, γ_{AMB} can be calculated from the range and azimuth distributed ambiguity ratios that are assumed equal in both interferometric channels:

$$\gamma_{AMB} = \frac{1}{1 + RASR} \cdot \frac{1}{1 + AASR} \tag{5}$$

The total coherence resulting from the above contributions is shown in Fig. 21 in black color. The plot also provides an overview of all individual coherence contributions. The AASR, which is constant versus incidence angle, causes the extensive flatness of the green colored ambiguity coherence curve.
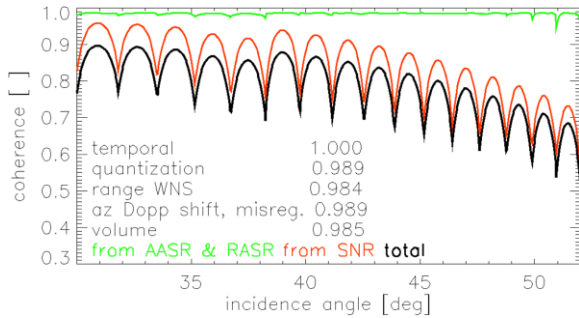

Fig. 21. Summary of all coherence contributions. The total coherence is the lowest curve in black color.

C. Interferometric Phase Error

The phase error is estimated by simulation. Input to the simulation is the total coherence and the number of interferometric looks, both dependent on the incidence angle. The swath overlap area is not included, and neither are the azimuth antenna pattern nor the sidelobe suppression considered.

The number of interferometric looks is shown in Fig. 22. It results from the ground resolution in the single look complex (SSC) image and the posting in the final DEM. The ground resolution was estimated in Section III.A.
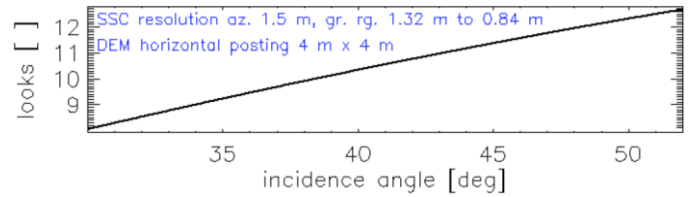

Fig. 22. Number of interferometric looks versus incidence angle.

The interferometric phase error for multiple looks is obtained by simulating two interferometric channels with a coherence equal to the total coherence described in the last subsection. Then, the required number of interferometric looks is generated and the multilook phase ψ_{ML} is measured according to [38]:

$$\psi_{ML} = Arg\left[\frac{1}{n} \cdot \sum_{k=1}^{n} S_i(k) \cdot S_j^*(k) \right], \tag{6}$$

with n being the number of interferometric looks, and S_i and S_j being the signals of the two interferometric channels with the simulated coherence. Fig. 23 provides in the top plot the measured Probability Density Function (PDF) of ψ_{ML} in black color.
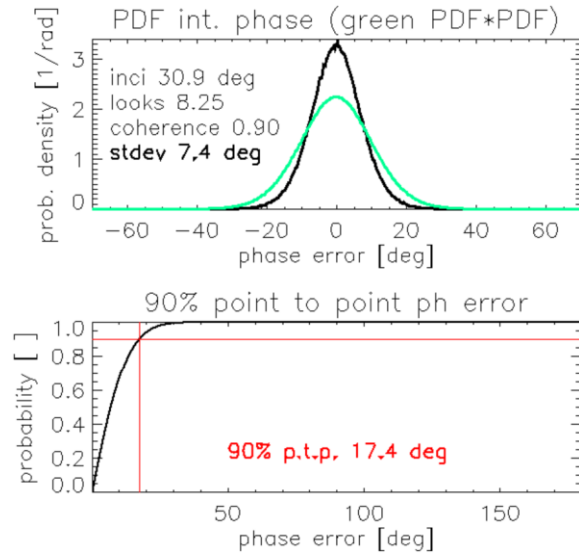

Fig. 23. (top) Probability density function (PDF) measured from phase noise simulation that is based on total coherence and number of interferometric looks. The green curve shows the convolution of the PDF with itself. (bottom) Cumulative probability distribution of the point-to-point phase error obtained from integration of the self-convolved PDF. The 90% point-to-point phase error is obtained from the probability curve.

In this plot, the standard deviation of ψ_{ML} for the annotated incidence angle, number of interferometric looks and coherence is 7.4°. In order to model the point-to-point phase error, the PDF is convolved with itself. The result is the green curve in the top plot of Fig. 23. From this, the 90% point-to-point phase error $\Delta\psi_{ML,90\%}$ is obtained by integration as shown in Fig. 23 on the bottom [19], [39]. For the annotated input parameter, $\Delta\psi_{ML,90\%}$ results to be 17.4°, which is 2.33 times the standard deviation.

D. Interferometric Height Error

The interferometric height error is finally obtained from the smallest HoA (cf. Fig. 15, right, bottom) and the interferometric phase error:

$$\Delta h_{ML,90\%} = \frac{\Delta \psi_{ML,90\%}}{2\pi} \cdot HoA \tag{7}$$

The smaller baseline allows for a high-quality phase unwrapping [46]. Fig. 24 shows the resulting point-to-point interferometric height error $\Delta h_{ML,90\%}$. For global coverage at the equator, a maximum incidence angle range from 30° to 48.2° is required. This is covered by the beams 0 to 12 as is discussed in the previous sections. The far range of beam 12 of 48.8° of incidence is indicated by the horizontal black dashed line in the figure.

Due to the convergence of the orbits with higher latitudes (c.f. Section VI.E below), the required incidence angle range for full coverage of circles of latitudes reduces. This allows to use only near range beams with better height performance. In Fig. 24, the white dashed curve provides the required far incidence angle for full coverage of all circles of latitudes. The near incidence angle is kept at 30° for all latitudes. Thus, the height error is below 2 m for all latitudes.
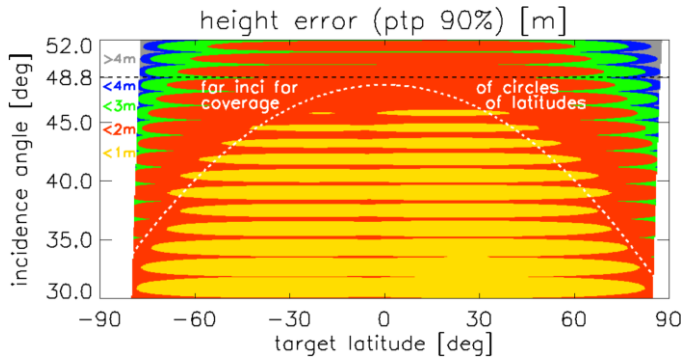

Fig. 24. Height error for a MirrorSAR satellites pointing error of 0.05° as a function of target latitude and incidence angle. The beams 0 to 12 that are required for global coverage at the equator range from 30° to 48.8° incidence angle. The white dashed curve provides the required far range incidence angle for full coverage of circles of latitude for all target latitudes. The near range incidence angle is always kept at 30°. If desired, one could also perform a second global acquisition with modified elevation beams that are shifted by half of the beam width as was done in TanDEM-X [19]. This would provide a height resolution better than 1 m with a posting of 4 m × 4 m globally.

The 2 m height performance is equal to the TanDEM-X mission, but at a horizontal posting of 4 m × 4 m. Compared to the 12 m × 12 m of TanDEM-X, this is a one order of magnitude improvement.

The baseline concept of Phase A provides room for optimization in the next mission phases as only one fixed baseline configuration was considered. For example, the height performance at higher latitudes can be further improved by introducing more flexible and complex baseline configurations. Moreover, at higher latitudes the number of beams required to cover the Earth reduces due to the convergence of the orbits and thus, beams with lower performance can be dropped.

A closer look to Fig. 24 reveals a periodic height error variation versus incidence angle. It is caused by the different elevation beams, that cover adjacent incidence angle sectors. In TanDEM-X, this variation has been counterbalanced by a half beamwidth offset of the second baseline acquisition with respect to the first one. This was possible since TanDEM-X acquired the second global baseline acquisition in a dedicated but also necessary second pass. For HRWS-MirrorSAR

alternative approaches to compensate for the height error variation are possible and are currently being considered.

Another way to visualize the expected performance improvement of HRWS-MirrorSAR with respect to TanDEM-X is to compare on a global scale the height error for an identical posting of 12 m x 12 m, which is the one of TanDEM-X. For generating the global height error maps, the TerraSAR-X global backscatter map [51] was used and a constant NESZ of -20 dB was set. The HoA was 20 m for HRWS-MirrorSAR and 35 m for TanDEM-X. Fig. 25 provides both global height error maps, expressed in terms of point-to-point 90% confidence error. The performance maps report also the mean value extracted from the distribution of the height errors over the global scale, i.e. 1.5 m for TanDEM-X and 0.6 m for HRWS-MirrorSAR.
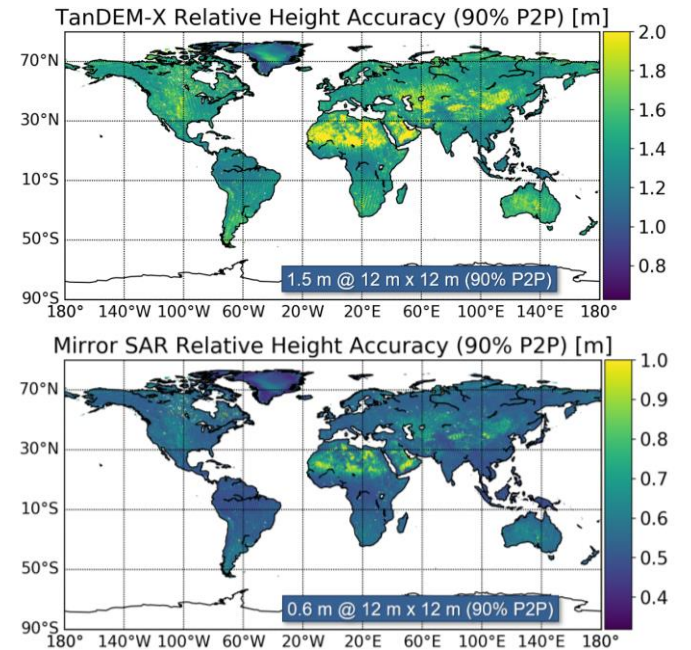

Fig. 25. Comparison of TanDEM-X (top) and HRWS-MirrorSAR (bottom) global height error map with identical posting of 12 m x 12 m. Note the smaller scale for the height error for HRWS-MirrorSAR. Of course, the posting of HRWS/MirrorSAR is better, the 12 m posting in the figure is just for the comparison with TanDEM-X.

E. Duration of DEM Acquisitions

One major goal of HRWS-MirrorSAR is the timely delivery of DEMs on local and regional scale. Hence, knowing the duration from ordering to completing the acquisition of a desired region of interest (ROI) is a central element. Observation strategies as well as on-demand services need to be designed accordingly. This subsection provides an approximation for the Duration from ordering to acquisition completion $D_{ROI,mean}$ of a ROI, which depends on the latitude Λ of a ROI and its extension in cross-track direction W_{ROI}.

HRWS shall fly a TerraSAR-X like orbit [1], which means a repeat cycle duration T_{RC} of 11 days and a total number of 167 repeating orbits within T_{RC}. This poses the requirement of a width of the Access Range (AR) of at least about 240 km ground range for achieving a gap free global coverage at the equator. With increasing latitude, the ARs overlap as is shown in Fig. 26.
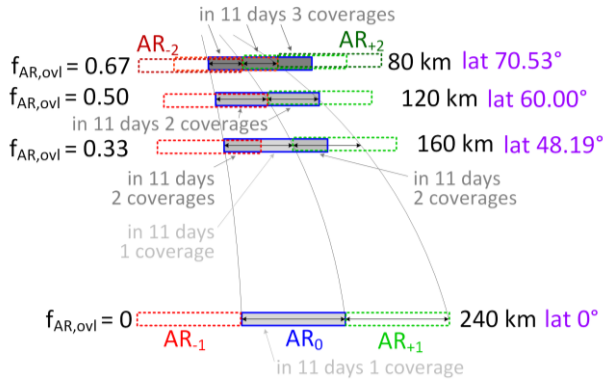
Fig. 26. Adjacent access ranges that correspond to adjacent repeating orbits in a repeat cycle. At the equator, the access ranges do not overlap. For increasing target latitude, the overlap increases, e.g., at 60° latitude, each position at the circle of latitude is covered twice. For 48° of latitude, half of the circle of latitude is covered twice, and half is covered only once.

The overlap of adjacent ARs is described by the overlap factor $f_{AR,ovl}$, which depends on the ROI's latitude Λ. Assuming a spherical Earth it can be approximated by

$$f_{AR,ovl} \approx 1 - \cos\Lambda \tag{8}$$

The following approximations and assumptions are made:
- Effective Swath Width SW_{eff} after subtraction of swath overlap is 19 km.
- Inclination is neglected and the cross-track AR at the equator is 240 km.
- Only ascending orbits or only descending orbits are considered.
- A general waiting margin T_{wait} is introduced. It includes the waiting time from ordering to acquisition, and also the time required to wait for other adjacent orbits. T_{wait} is set to $T_{RC}/2$ independent off latitude and W_{DEM}. This approximation is considered sufficient for the duration estimation in Phase A.
- The required number of swathes N_{SW} is cut-off at 13, which covers 240 km at the equator. A fractional required swath counts as full swath and N_{SW} is an integer number. In (9), $\lceil \; \rceil$ is the ceiling function.

$$N_{SW} = \lceil W_{DEM} / SW_{eff} \rceil \; \leq \; 13 \tag{9}$$

- From Fig. 26, a Mean Multi Coverage factor M_{MC} can be derived that depends on latitude.

$$M_{MC} = \frac{1}{1 - f_{AR,ovl}} = \frac{1}{\cos\Lambda} \tag{10}$$

With the above approximations and assumptions, D_{ROI} can be expressed by (11) up to a W_{ROI} of 247 km. For a larger W_{ROI} up to global coverage, the duration prolongs by one T_{RC}.

$$D_{ROI} \approx (N_{SW} - 1) \cdot T_{RC} \cdot M_{MC}^{-1} + T_{wait} \quad \text{for } W_{ROI} \leq 247\ km$$
$$D_{ROI} \approx 13 \cdot T_{RC} \cdot M_{MC}^{-1} + T_{wait} \qquad \text{for } W_{ROI} > 247\ km \tag{11}$$

Fig. 27 provides the according D_{ROI} as a function of W_{ROI} for different latitudes. At the equator, a small W_{ROI} up to 19 km has from ordering to acquisition completion a duration of 5.5 days, a W_{ROI} up to 38 km lasts 11+5.5 = 16.5 days, and a W_{ROI} of up to 247 km lasts 4.58 months.
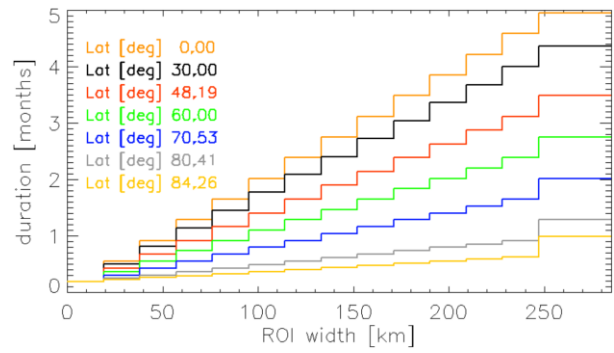

Fig. 27. Duration versus ROI width. Best location case (dotted line).

In order to show more concrete acquisition examples at different latitudes, two ROI scenarios are analyzed: a large ROI coverage of Nigeria at an average latitude of 9°N and a medium ROI coverage of Lebanon at an average latitude of 34°N. As is depicted in Fig. 28, Nigeria has a W_{ROI} of 1300 km. According to (11), the duration is estimated to 4.9 months. Lebanon has a W_{ROI} of 140 km, which means a N_{SW} of 8 beams. The resulting duration is 69 days or 2.3 months. Note the effect of the latitude.

Fig. 28. Coverage scenario of Nigeria (left) and Lebanon (right) including necessary orbits and first data-take beams. (Maps from Google Earth)

It is important to be aware that the durations D_{ROI} are for an ideal case where the orbit duty cycle is fully available to the DEM acquisition. The orbit duty cycle shared between DEM and exclusive HRWS acquisitions will be traded in the upcoming mission phases including the operations phase. However, the D_{ROI} estimates in this section are realistic for smaller ROI. For larger ROI, the duration may become longer. In an ideal case with full access to the orbit duty cycle by the DEM acquisition, a global acquisition can be achieved in about 5 months. Assuming the same orbit duty cycle available for DEM acquisitions as in the TanDEM-X mission, a global DEM can be acquired within about 2 years.

VII. CONCLUSIONS

This paper presents the results of the HRWS-MirrorSAR Phase A study. MirrorSAR adds to the HRWS mission a single-pass multi-baseline interferometric capability. This allows the generation of a DEM with a performance improved by one order of magnitude compared to TanDEM-X. Three transponder-like MirrorSAR satellites fly a triple helix orbit formation around the HRWS orbit and forward their radar signals received from ground via the MirrorLink to the HRWS satellite that hosts the full radar receiving chain.

For HRWS-MirrorSAR, the double mirror link was selected with three different carrier frequencies slightly higher than the X-band radar frequency. This allows to exploit the large HRWS receive bandwidth. The MirrorLink will be further optimized, simulated and demonstrated in the next mission phases.

Initial system engineering analysis resulted in 15 elevation beams of 20 km width that overlap by 1 km, and a SAR receive antenna size on-board the MirrorSAR satellites of 3 m in azimuth and about 1 m in elevation. The SAR performance was estimated based on these fundamental system parameters.

Global coverage is provided by the beams 0 to 12 that cover 30° to 48.8° incidence angle. One major outcome of the SAR performance analysis is a required pointing accuracy of 0.05° for the MirrorSAR satellites. The driver in the pointing analysis was the azimuth ambiguity performance. One recommendation to the next mission phases is the introduction of more advanced ambiguity suppression techniques. DEM performance as presented in this paper treats azimuth ambiguities as incoherent noise only. Further mission phases should include a distinction between coherent and incoherent ambiguities. There is ongoing research work on this topic.

The antenna pattern design on which the performance is based was rather straight forward in Phase A. A refinement and joint consideration of orbit formation design and SAR performance as well as height performance is expected to further enhance the overall interferometric system performance.

One fundamental outcome of the MirrorLink analysis is that its beamwidth depends on the relative satellite positions within the formation as well as on the applied Doppler steering laws. Total Zero Doppler Steering has been assumed in the Phase A study. In the meantime, a dedicated Doppler steering approach for multistatic satellite formations [32] is available that should be included into the mission.

In terms of echo window timing, the monostatic nadir area was extended to a forward reflection area, which describes the location of the strongest direct reflections outside the desired swath in bistatic acquisitions. The additional signal delay along the MirrorLink has been included. A main finding was that a Pulse Repetition Interval limitation on the length of the recorded echo lines on-board HRWS establishes zones of allowed and forbidden along-track separations between the HRWS satellite and the MirrorSAR satellite formation.

The large horizontal Rx baseline was defined to be 1300 m at the equator. This provides the required 2 m height accuracy at a posting of 4 m × 4 m at all latitudes visible from the orbit. The corresponding height of ambiguity at the equator is below 20 m. The smallest baseline required for high quality phase unwrapping was set to 200 m at the equator considering the need of a safe orbit formation. Simulations showed that the DEM required height error better than 2 m was achieved at the horizontal posting of 4 m × 4 m in both ground dimensions. Note that only one orbital baseline configuration was analyzed. In the next mission steps, the baseline design will be further elaborated, to further improve the height error performance.

The expected acquisition duration was analyzed for several scenarios that differentiate small, medium, and large regions of interest to be acquired. In an ideal case with full access to the orbit duty cycle, a dedicated global DEM acquisition is expected to last about 5 months. Assuming an available orbit duty cycle as in the TanDEM-X mission, which corresponds to a rather realistic case, a global DEM acquisition can be made in about 2 years.

In summary, HRWS-MirrorSAR incorporates several innovations that provide an order-of-magnitude performance improvement over the high-quality and well-established DEM of the TanDEM-X mission.

APPENDIX: SIMULATION OF EXPECTED DEM PERFORMANCE

As discussed in Section VI.C, HRWS-MirrorSAR shall deliver a DEM with a horizontal posting of 4 m × 4 m at a 90% point-to-point vertical accuracy better than 2 m globally. This appendix intends to illustrate the quality improvement of such maps in comparison to currently available alternatives such as the TanDEM-X global DEM (12 m posting, point-to-point vertical accuracy better than 2 m) and SRTM (30 m posting, point-to-point vertical accuracy better than 10 m). For that purpose, we use data acquired by DLR's airborne SAR sensor, the F-SAR [49], a multi-frequency SAR system often used to demonstrate techniques later implemented in spaceborne missions. For the results presented in this section, data obtained with the X-band single-pass configuration were used. The imaged scene is Kaufbeuren, in Germany, the standard calibration site for F-SAR data, an area which contains flat to moderate terrain.

A simple methodology was employed for generating DEMs with different resolution and relative vertical accuracies. First, the F-SAR interferogram was spatially averaged using a rectangular convolution kernel with sizes of a) 30 m × 30 m, b) 12 m × 12m and c) 4 m × 4 m. After averaging, the data were given as input to the F-SAR DEM generation chain [50]. Finally, synthetic noise was added to each product in order to match point-to-point relative accuracies of a) 10 m, b) 2 m and c) 2 m. Note that the simulated DEMs match worst-case scenarios expected for a) SRTM/SIR-C, b) TanDEM-X and c) HRWS-MirrorSAR. Moreover, the post-processing of the F-SAR products is possible since the original interferogram has a mean coherence of 0.92 and a mean height of ambiguity of around 60 m, i.e., the expected height 90% point-to-point error is well below 2 m for the considered resolutions (number of independent looks is larger than 125 in all cases).

Fig. 2 shows exemplarily, from top to bottom, shaded relief images of the obtained raw DEMs regarding the simulated cases a) SRTM-/SIR-C, b) TanDEM-X, and c) HRWS-MirrorSAR. Raw DEM means here that the DEM is non-edited and is obtained from a single pass. The increased details of case c) w.r.t. case b) are apparent, especially over the urban area. This can even be better seen in the region within the black rectangle in the second plot. A zoom of that region is shown in Fig. 3 for the simulated SRTM/SIR-C and HRWS-MirrorSAR cases.

REFERENCES

[1] J. Janoth, M. Jochum, L. Petrat, and T. Knigge, "High Resolution Wide Swath – the next Generation X-band mission", Proc. of IGARSS 2019.

[2] M. Bartusch, A. Nuncio Quiroz, S. Stettner, A. Moreira, and M. Zink, "German X-band Spaceborne SAR Heritage and the Future HRWS Mission", in Proc. IGARSS, Brussels, Belgium, 2021.

[3] A. Currie and M. A. Brown, "Wide-swath SAR," IEE Proceedings F - Radar and Signal Processing, vol. 139, pp. 122-135, 1992.

[4] M. Suess, B. Grafmueller, and R. Zahn, "A novel high resolution, wide swath SAR system," in Proc. IEEE Geoscience and Remote Sensing Symposium, Sydney, Australia, pp. 1013-1015, 2001.

[5] N. Gebert, G. Krieger, and A. Moreira. "Digital beamforming on receive: Techniques and optimization strategies for high-resolution wide-swath SAR imaging." IEEE Transactions on Aerospace and Electronic Systems 45.2 (2009): 564-592.

[6] N. Gebert, G. Krieger, and A. Moreira. "Multichannel azimuth processing in ScanSAR and TOPS mode operation." IEEE Transactions on Geoscience and Remote Sensing 48.7 (2010): 2994-3008.

[7] G. Dieterle, F. Schlude, "The European MRSE-Project on the first Spacelab Flight", Proc. IGARSS'82, Munich, Germany

[8] A. Freeman, M. Zink, E. Caro, A. Moreira, L. Veilleux, and M. Werner, "The legacy of the SIR-C/X-SAR radar system: 25 years on". Remote Sensing of Environment, 231, 111255, 2019.

[9] E. Stofan, D. Evans, C. Shmullius, B. Holt, J. Plaut, J. van Zyl, S. Wall, and J. Way, "Overview of Results of Spaceborne imaging Radar-C, X-Band Synthetic Aperture Radar (SIR-C/X-SAR), IEEE TGRS, Vol. 33, No. 4, July 1995.

[10] M. Werner, "The X-band synthetic aperture radar on-board the space shuttle", Proc. Third Spaceborne Imaging Radar Symp., Jan. 18-21, 1993, pp. 67-73.

[11] J. Moreira et al., „X-SAR interferometry: First results", IEEE TGRS, Vol. 33, No. 4, July 1995.

[12] M. Werner, "Shuttle Radar Topography Mission (SRTM): Experience with the X-Band SAR Interferometer", Proceedings of CIE International Conference on Radar, 2001.

[13] E. Rodriguez, C.S. Morris, J.E. Belz, E.C. Chapin, J. M. Martin, W. Daffer, S. Hensley, "An Assessment of the SRTM Topographic Products", Online https://www2.jpl.nasa.gov/srtm/SRTM_D31639.pdf

[14] R. Werninghaus and S. Buckreuss, "The TerraSAR-X mission and system design," IEEE Trans. Geosci. Remote Sens., vol. 48, no. 2, pp. 606–614, Feb. 2010.

[15] W. Pitz, and D. Miller, "The TerraSAR-X Satellite", IEEE Trans. Geosci. Remote Sens., vol. 48, no. 2, pp. 615–622, Feb. 2010.

[16] J. Mittermayer, M. Younis, R. Metzig, S. Wollstadt, J. M. Martinez, and A. Meta, "TerraSAR-X system performance characterization and verification," IEEE Trans. Geosci. Remote Sens., vol. 48, no. 2, pp. 660–676, Feb. 2010.

[17] J. Mittermayer, S. Wollstadt, P. Prats-Iraola, and R. Scheiber, "The TerraSAR-X staring spotlight mode concept," *IEEE Trans. Geosci. Remote Sens.*, vol. 52, no. 6, pp. 3695–3706, Jun. 2014.

[18] T. Kraus, B. Bräutigam, J. Mittermayer, S. Wollstadt, and C. Grigorov, "TerraSAR-X Staring Spotlight Mode Optimization and Global Performance Predictions", IEEE J. of Selected Topics in Applied Earth Observations and Remote Sensing, Vol. 9, No. 3, 2016.

[19] G. Krieger, A. Moreira, H. Fiedler, I. Hajnsek, M. Werner, M. Younis, and M. Zink, "TanDEM-X: A Satellite Formation for High Resolution SAR Interferometry", IEEE Transactions on Geoscience and Remote Sensing, vol. 45, no. 11, pp. 3317 – 3341, 2007.

[20] M. Zink, A. Moreira, I. Hajnsek, P. Rizzoli, M. Bachmann, R. Kahle, T. Fritz, M. Huber, G. Krieger, M. Lachaise, M. Martone, E. Maurer, and B. Wessel: "TanDEM-X: 10 Years of Formation Flying Bistatic SAR Interferometry", IEEE Journal of Selected Topics in Applied Earth Observations and Remote Sensing, Vol. 14, pp. 3546-3565, 2021.

[21] P. Rizzoli et al., "Generation and performance assessment of the global TanDEMX digital elevation model," ISPRS J. Photogrammetry Remote Sens., vol. 73, pp. 119–139, 2017.

[22] M. Lachaise, B. Schweißhelm, T. Fritz, "The New TanDEM-X Change DEM: Specification and Interferometric Processing", Proc of IEEE Latin American GRSS & ISPRS Remote Sensing Conference (LAGIRS), 2020.

[23] G. Krieger et al., "MirrorSAR: A Fractionated Space Radar for Bistatic, Multistatic and High-Resolution Wide-Swath SAR Imaging," in Proc. IGARSS, Fort Worth, Texas, USA, 2017.

[24] G. Krieger, M. Zonno, J. Mittermayer, A. Moreira, S. Huber, and M. Rodriguez-Cassola, "MirrorSAR: A Fractionated Space Transponder

[25] M. Zonno, M. Rodriguez-Cassola, G. Krieger, A. Moreira, F. Lopez-Dekker, "Synthetic Aperture Radar Method and Synthetic Aperture Radar System", European Patent EP3425422, Jan. 9, 2019.

[26] M. Zonno, G. Krieger, M. Rodriguez-Cassola, J. Mittermayer, and A. Moreira, "A MirrorSAR-based single-pass dual-baseline SAR interferometer for the generation of very high quality DEMs", Proc. of EUSAR 2018, Aachen, 2018.

[27] J. Mittermayer, G. Krieger, A. Bojarski, M. Zonno, M. Villano, and A. Moreira, "A MirrorSAR Case Study Based on the X-Band", Proc. of EUSAR 21, On-line, Germany.

[28] J. Mittermayer, G. Krieger, and A. Moreira, „Concepts and Applications of Multistatic MirrorSAR Systems", Proc. of IEEE Radar 20, Florence, Italy.

[29] J. Mittermayer, G. Krieger, M. Villano, and A. Moreira, "A Novel MirrorSAR Concept for Augmenting the Next German Synthetic Aperture Radar Mission HRWS with Single-Pass Interferometry", Proc. of the 13th IAA Symposium on Small Satellites for Earth Observation 2021, Berlin, Germany.

[30] F. T. Ulaby and M. C. Dobson, "Handbook of Radar Scattering Statistics for Terrain". Norwood, MA: Artech House, 1989.

[31] J. Mittermayer, M. Younis, R. Metzig, S. Wollstadt, J. M. Martinez, and A. Meta, "TerraSAR-X system performance characterization and verification," *IEEE Trans. Geosci. Remote Sens.*, vol. 48, no. 2, pp. 660–676, Feb. 2010.

[32] J. Mittermayer, G. Krieger, and S. Wollstadt, "Numerical Calculation of Doppler Steering Laws in Bi- and Multistatic SAR", IEEE TGRS 2021 (Early Access), DOI 10.1109/TGRS.2021.3058554.

[33] S. Wollstadt and J. Mittermayer, "Nadir Margins in TerraSAR-X Timing Commanding", Proc. of CEOS SAR Calibration and Validation Workshop, 2008.

[34] G. Krieger, A. Moreira, "Multistatic SAR Satellite Formations: Potentials and Challenges", Proc. of IGRARSS 2005.

[35] H. Fiedler, E. Boerner, J. Mittermayer, and G. Krieger, "Total zero Doppler steering—A new method for minimizing the Doppler centroid," IEEE Geosci. Remote Sens. Lett., vol. 2, no. 2, pp. 141–145, Apr. 2005.

[36] A. Moreira, G. Krieger, and J. Mittermayer, "Satellite configuration for interferometric and/or tomographic remote sensing by means of synthetic aperture radar (SAR)," U.S. Patent 6 677 884, U.S. Off. Pat. Office, Washington, DC, Jul. 2002.

[37] D. Just and R. Bamler, "Phase statistics of interferograms with applications to synthetic aperture radar," *Appl. Opt.*, vol. 33, no. 20, pp. 4361–4368, Jul. 1994.

[38] J.-S. Lee, K. W. Hoppel, S. A. Mango, and A. R. Miller, "Intensity and phase statistics of multilook polarimetric and interferometric SAR imagery," *IEEE Trans. Geosci. Remote Sens.*, vol. 32, no. 5, pp. 1017–1028, Sep. 1994.

[39] A. Papoulis, Probability, Random Variables, and Stochastic Processes. New York: McGraw-Hill, 1991

[40] M. Villano and G. Krieger, "Impact of Azimuth Ambiguities on Interferometric Performance," IEEE Geoscience and Remote Sensing Letters, vol. 9, no. 5, pp.896-900, Sept. 2012.

[41] M. Villano and G. Krieger, "Accounting for Azimuth Ambiguities in Interferometric Performance Analysis," IEEE International Geoscience and Remote Sensing Symposium (IGARSS) 2012, Munich, Germany, 22-27 July 2012.

[42] N. Ustalli and M. Villano, "Impact of Ambiguity Statistics on Information Retrieval for Conventional and Novel SAR Modes," Proceedings of the IEEE 2020 Radar Conference, Florence, Italy, 21-25 September 2020.

[43] A.Monti Guarnieri, "Adaptive removal of azimuth ambiguities in SAR images," IEEE Trans. Geosci. Remote Sens., vol. 43, no. 3, pp. 625–633, Mar. 2005.

[44] M. Villano and G. Krieger, "Spectral-Based Estimation of the Local Azimuth Ambiguity-to-Signal Ratio in SAR Images," IEEE Transactions on Geoscience and Remote Sensing, vol. 52, no. 5, pp. 2304-2313, May 2014.

[45] D. Borla Tridon, M. Bachmann, D. Schulze, C. Ortega-Míguez, M. Polimeni, M. Martone, J. Böer, and M. Zink "TanDEM-X: DEM Acquisition in the third Year Era." International Journal of Space Science and Engineering, 2014, 1 (4), pp 367-381. InderScience Publishers. doi: 10.1504/IJSPACESE.2013.059270. ISBN 2048-8459. ISSN 2048-8459.

[46] M. Bachmann, T. Kraus, A. Bojarski, M. Schandri, J. Böer, T. Busche, J. L. Bueso Bello, C. Grigorov, U. Steinbrecher, S. Buckreuss, G. Krieger, and M. Zink "The TanDEM-X Mission Phases - Ten Years of Bistatic

Acquisition and Formation Planning" ,IEEE Journal of Selected Topics in Applied Earth Observations and Remote Sensing, IEEE - Institute of Electrical and Electronics Engineers, 2021, ISSN 1939-1404.

[47] M. Martone, P. Rizzoli, and G. Krieger, "Volume Decorrelation Effects in TanDEM-X Interferometric SAR Data", IEEE GRL, Vol. 13, No. 12, 2016.

[48] M. Lachaise, T. Fritz, and H. Breit, "InSAR processing and dual-baseline phase unwrapping for global TanDEM-X DEM generation," in *Proc. IEEE Geosci. Remote Sens. Symp. (IGARSS)*, 2014, pp. 2229–2232.

[49] A. Reigber et al., "Very-high-resolution airborne synthetic aperture radar imaging: Signal processing and applications, "Proceedings of the IEEE, vol. 101, no. 3, pp. 759–783, 2012.

[50] M. Pinheiro et al., "Generation of highly accurate DEMs over flat areas by means of dual-frequency and dual-baseline airborne SAR interferometry", IEEE Transactions on Geoscience and Re-mote Sensing, vol. 56, no. 8, pp. 4361–4390, 2018.

[51] P. Rizzoli, B. Bräutigam, S. Wollstadt, and Josef Mittermayer, "Radar Backscatter Mapping Using TerraSAR-X", IEEE Trans. Geosci. Remote Sens., vol. 49, no. 10, pp. 3538–3547, Feb. 2011.

Josef Mittermayer received the Dipl.-Ing. (M.Sc.) degree in electrical engineering from the Technical University of Munich, Munich, Germany, in 1995, the M.Sc. degree in space system engineering from the Delft University of Technology, Delft, The Netherlands, in 2004, and the Ph.D. degree from the University of Siegen, Siegen, Germany, in 2000.

Since 1994 he is with the Microwaves and Radar Institute, German Aerospace Center (DLR), Oberpfaffenhofen, Germany. From 2002 to 2008 he worked in the TerraSAR-X project, from 2004 to 2008 also in the TerraSAR-X group leader position. Additionally, he was the project manager of *TerraSAR-X System Engineering and Calibration*, and was technically responsible for the TerraSAR-X commissioning phase. His scientific and engineering work includes the fields SAR processing, SAR system engineering, and SAR mode development. Currently, NewSpace and formations of small multistatic SAR satellites is a focus of his work. Apart from numerous conference papers and patents in the field of SAR, Dr. Mittermayer is author or co-author of more than 20 peer-reviewed journal papers.

Dr. Mittermayer and his colleagues were recipients of the IEEE Geoscience and Remote Sensing Society Transactions Prize Paper Award for a paper on air and spaceborne stripmap and ScanSAR processing in 1996. He was a recipient of the DLR Science Award in 2001 for his work on spotlight-SAR processing. In 2011, he was awarded with the DLR *Forschungssemester* for his contribution to the TerraSAR-X project.

Gerhard Krieger (M'04-SM'09-F'13) received the Dipl.-Ing. (M.S.) and Dr.-Ing. (Ph.D.) (Hons.) degrees in electrical and communication engineering from the Technical University of Munich, Germany, in 1992 and 1999, respectively.

From 1992 to 1999, he was with the Ludwig Maximilians University, Munich, where he conducted multidisciplinary research on neuronal modeling and nonlinear information processing in biological and technical vision systems. Since 1999, he has been with the Microwaves and Radar Institute of the German Aerospace Center (DLR), Oberpfaffenhofen, Germany, where he started as a research associate developing signal processing algorithms for a novel forward-looking radar system employing digital beamforming on receive. From 2001 to 2007, he led the New SAR Missions Group which pioneered the development of advanced bistatic and multistatic radar systems, such as TanDEM-X, as well as innovative multichannel SAR techniques and algorithms for high-resolution wide-swath SAR imaging. Since 2008, he has been the Head of the Radar Concepts Department which hosts about 40 scientists focusing on new SAR techniques, missions and applications. He has moreover been serving as Mission Engineer for TanDEM-X and he made also major contributions to the development of the Tandem-L mission concept, where he led the Phase-0 and Phase-A studies. Since 2019, he is moreover a professor at the Friedrich-Alexander-University Erlangen, Germany. Gerhard Krieger is author or co-author of more than 100 peer-reviewed journal papers, 9 invited book chapters, more than 400 conference papers, and more than 20 patents.

Prof. Krieger has been an Associate Editor for the IEEE Transactions on Geoscience and Remote Sensing since 2012. In 2014, he served as the Technical Program Chair for the European Conference on Synthetic Aperture Radar and as a Guest Editor for the IEEE Journal of Selected Topics in Applied Earth Observations and Remote Sensing. He received several national and international awards, including two Best Paper Awards at the European Conference on Synthetic Aperture Radar, two Transactions Prize Paper Awards of the IEEE Geoscience and Remote Sensing Society, and the W.R.G. Baker Prize Paper Award from the IEEE Board of Directors.

Allan Bojarski received the Dipl. -Ing. degree in aerospace engineering from the Technical University of Munich (TUM), Munich, Germany, in 2014.

After 2 years performing battery simulations for the Daimler R&D department in Ulm, Germany, in 2016 he joined the Microwaves and Radar Institute at the German Aerospace Center (DLR) in Oberpfaffenhofen, Germany. He is currently involved in various spaceborne SAR projects as a mission engineer. In this context, he is responsible for the long-term system monitoring of TerraSAR-X/TanDEM-X satellites and the scientific acquisition planning for the TanDEM-X mission. Furthermore, he is designing mission scenarios, SAR satellite formations and observation concepts for several SAR missions such as Tandem-L or HRWS.

Mariantonietta Zonno was born in Bari, Italy, in 1986. She received the M.S. degree (with Hons.) in telecommunication engineering from the Politecnico di Bari, Bari, in 2011, and the PhD degree jointly from the Scuola Interpolitecnica di Dottorato, Turin, Italy, and the Politecnico di Bari, in 2015. During her PhD studies, she visited the Microwaves and Radar Institute, German Aerospace Center, Wessling, Germany, for eight months.

Since 2014, she has been with the SAR Mission Group, Microwaves and Radar Institute, German Aerospace Center. Her research interests include the study of future SAR missions' concepts and analysis of the mission performance.

Michelangelo Villano (Senior Member, IEEE) received the B.Sc. and M.Sc. degrees (Hons.) in telecommunication engineering from the Sapienza University of Rome, Rome, Italy, in 2006 and 2008, respectively, and the Ph.D. degree (Hons.) in electrical engineering and information technology from the Karlsruhe Institute of Technology, Karlsruhe, Germany, in 2016.

From 2008 to 2009, he was a Young Graduate Trainee with the European Space Research and Technology Center, European Space Agency, Noordwijk, The Netherlands, where he developed processing algorithms for ice sounding radar. In 2017, he was a Visiting Research Scientist with the Communications, Tracking, and Radar Division, NASA Jet Propulsion Laboratory, Pasadena, CA, USA, where he analyzed novel acquisition modes for the NASA Indian Space Research Organization synthetic aperture radar (SAR) instrument. Since 2009, he has been with the German Aerospace Center (DLR), Microwaves and Radar Institute, Wessling, Germany, where he is currently the Head of the NewSpace SAR Research Group. Since 2019, he has also been a Lecturer with Ulm University, Ulm, Germany. He has authored or coauthored nearly 100 research articles in peer-reviewed journals and international conference proceedings. He holds nine patents in the field of SAR. His research interests include the conception of innovative SAR modes for high-resolution wide-swath imaging and the development of low-cost SAR solutions for frequent and enhanced Earth monitoring.

Dr. Villano has been a member of technical program committee for several international conferences and workshops. He was a recipient of the First Place Student Paper Award at the European Conference on SAR (EUSAR), Berlin, Germany, in 2014, the IEEE Geoscience and Remote Sensing Society Letters

This article has been accepted for publication in a future issue of this journal, but has not been fully edited. Content may change prior to final publication. Citation information: DOI 10.1109/TGRS.2021.3132384, IEEE Transactions on Geoscience and Remote Sensing

>TGRS-2021<

18

Prize Paper Award in 2015 and 2017, the Student Paper Award at the Asia–Pacific Conference on Synthetic Aperture Radar, Marina Bay Sands, Singapore, in 2015, the DLR Science Award in 2016, the Award as Young Scientist of the Foundation Werner von Siemens Ring in 2017, the ITG Dissertation Award in 2017, and the Best Paper Award at the German Microwave Conference 2019. He is co-chair of the Working Group on Remote Sensing Instrument and Technologies for Small Satellites of the IEEE Geoscience and Remote Sensing Society's Technical Committee on Instrumentation and Future Technologies. He serves as an Associate Editor for the IEEE GEOSCIENCE AND REMOTE SENSING LETTERS. He has served as a Guest Editor for the special issues Advances in Antenna Array Processing for Radar 2014 and Advances in Antenna Array Processing for Radar 2016 of the International Journal of Antennas and Propagation.

Muriel Pinheiro received the B.S. degree in electronic engineering and the M.S. degree in telecommunications from Aeronautical Technological Institute, So Jos dos Campos, Brazil, in 2009 and 2010, respectively, and the Dr-Ing. degree (hons.) from the Karlsruhe Institute of Technology, Karlsruhe, Germany, in 2016.

From 2009 to 2010, she was at BRADAR, working with the development of calibration algorithms for airborne SAR interferometry. From 2011 to 2021, she was at the Microwaves and Radar Institute of the German Aerospace Center, Wessling, Germany (DLR), where she was a member of the Multimodal Algorithms Group. Her research topics included signal and image processing, advanced techniques for SAR image formation, end-to-end SAR simulation, SAR interferometry, high resolution DEM generation and persistent scatterer interferometry.

Since 2021 she has joined the European Space Agency (ESA), Frascati, as calibration and validation engineer for SAR missions, with special focus on the quality assurance of Sentinel-1 products.

Markus Bachmann received the Dipl.-Ing. degree and his PhD degree in electrical engineering from the Technical University of Karlsruhe, Germany, in 2005 and 2015 respectively.

In 2005 he joined the Microwaves and Radar Institute at the German Aerospace Center. From 2005 to 2011 he was in charge of the implementation and calibration of the TerraSAR-X/TanDEM-X antenna model. From 2006 to 2010 he assessed the potentials and methods of the DEM calibration for TanDEM-X. From 2008 to 2010 he was responsible for the planning and execution of the TanDEM-X commissioning phase. Between 2011 and 2014 he performed the interferometric and radargrametric calibration of the TanDEM-X system and established the monitoring of the global coverage for the TanDEM-X mission. He is ground segment project manager of the Tandem-L/Rose-L-Tandem project since 2016.

Since 2012, he is head of the Mission Engineering group, which is in charge of the operational planning of the bistatic acquisitions for TanDEM-X and for future missions like Tandem-L, Rose-L Tandem or HRWS as well as for the analysis of mission relevant aspects in the frame of various SAR missions.

Stefan Buckreuss received the Dipl.-Ing. degree in electronics from the Technical University of Munich, Munich, Germany in 1988 and the Dr.-Ing. degree from the University of Stuttgart, Stuttgart, Germany in 1994.

He has been with the Deutsches Zentrum für Luft- und Raumfahrt (DLR), Microwaves and Radar Institute, Oberpfaffenhofen, Germany since 1988 where he gained broad experience in SAR signal processing, motion compensation, anti-jamming and interferometry. Since 2002 he is engaged in the German TerraSAR-X/TanDEM-X mission where he was responsible for the development of the instrument operations and calibration segment until he was assigned the role of the ground segment integration manager. He is currently the TerraSAR-X and TanDEM-X mission manager responsible for the general mission aspects.

Alberto Moreira (M'92, S'96, F'04) received the BSEE and MSEE degrees from the Aeronautical Technological Institute (ITA), São José dos Campos, in 1984 and 1986, respectively, and the Eng. Dr. degree (with honors) from the Technical University of Munich, Germany, in 1993. From 1996 to 2001, he was the head of the SAR Technology Department, German Aerospace Center (DLR), Oberpfaffenhofen, Germany. Under his leadership, the DLR airborne SAR system has been upgraded to operate in innovative imaging modes like polarimetric SAR

interferometry, tomography and holography. Since 2001, Prof. Moreira is the Director of the Microwaves and Radar Institute at DLR and a Full Professor with the Karlsruhe Institute of Technology (KIT), in the field of microwave remote sensing. His DLR's Institute contributes to several scientific programs and projects for spaceborne SAR missions like TerraSAR-X, TanDEM-X, HRWS, SAR-Lupe and SARah as well as Kompsat-6, PAZ, Sentinel-1, BIOMASS, ROSE-L, Harmony, Sentinel-1NG and VERITAS. The mission TanDEM-X, led by his Institute, has generated a global, high-resolution digital elevation model of the Earth with unprecedented accuracy. Prof. Moreira is the initiator and principal investigator (PI) for this mission. His professional interests and research areas encompass spaceborne radar end-to-end system design, microwave techniques and system concepts, signal processing, and remote sensing applications.

Prof. Moreira is author or co-author of more than 450 publications in international conferences and journals, 8 book chapters, and holds more than 40 international patent grants in the radar and antenna field. He is an IEEE fellow and has served as President of the IEEE Geoscience and Remote Sensing (GRS) Society in 2010 as well as General Co-Chair of IGARSS in 2012. He was founder and chair of the GRSS German Chapter (2003-2008), served as Associate Editor for the IEEE GRS Letters (2003-2007) and for the IEEE TGRS (since 2005), and is serving as chair of the Major Awards of the GRS society since 2017. He is recipient of several international awards including the IEEE AESS Nathanson Award (1999) for the "Young Radar Engineer of the Year", the IEEE Kiyo Tomiyasu Field Award (2007), IEEE W.R.G. Baker Award from the IEEE Board of Directors (2012), and the IEEE GRSS Distinguished Achievement Award (2014). He and his colleagues received the GRSS Transactions Prize Paper Awards in 1997, 2001, and 2007 and the GRSS Letters Prize Paper Award in 2015 and 2017. From 2012 to 2018 he has served as principal investigator for the Helmholtz Alliance "Remote Sensing and Earth System Dynamics" in support of Tandem-L, a radar mission proposal for the global observation of dynamic processes on Earth's surface with unprecedented quality and resolution.